硕士学位论文

参数化哈密顿量特征向量和特征值构型的拓扑

TOPOLOGY OF THE CONFIGURATION OF EIGENVECTORS AND EIGENVALUES OF PARAMETRIZED HAMILTONIANS

研　　究　　生：方舟

指　导　教　师：朱一飞助理教授

南方科技大学

二〇二六年五月

国内图书分类号：O469　　学校代码：14325
国际图书分类号：53.01　　密级：公开

理学硕士学位论文

参数化哈密顿量特征向量和特征值的构型的拓扑

学 位 申 请 人：方舟
指　导　教　师：朱一飞助理教授
学　科　名　称：量子科学与工程
答　辩　日　期：2026 年 5 月
培　养　单　位：量子科学与工程研究院
学位授予单位：南方科技大学

TOPOLOGY OF THE CONFIGURATION OF EIGENVECTORS AND EIGENVALUES OF PARAMETRIZED HAMILTONIANS

A dissertation submitted to
Southern University of Science and Technology
in partial fulfillment of the requirement
for the degree of
Master of Science
in
Quantum Science and Engineering

by
Fang Zhou

Supervisor: Assistant Prof. Yifei Zhu

May, 2026

学位论文公开评阅人和答辩委员会名单

公开评阅人名单

XX	教授	南方科技大学
XX	副教授	XXXX 大学
XX	研究员	中国 XXXX 科学院 XXXXXXX 研究所

答辩委员会名单

主席	李展	副教授	南方科技大学
委员	胡晓文	副教授	大湾区大学
	卢海舟	教授	南方科技大学
秘书	王甫东	博士后	南方科技大学

DECLARATION OF ORIGINALITY AND AUTHORIZATION OF THESIS, SOUTHERN UNIVERSITY OF SCIENCE AND TECHNOLOGY

Declaration of Originality of Thesis

I hereby declare that this thesis is my own original work under the guidance of my supervisor. It does not contain any research results that others have published or written. All sources I quoted in the thesis are indicated in references or have been indicated or acknowledged. I shall bear the legal liabilities of the above statement.

Signature: [redacted] Date: 2026.5.25

Declaration of Authorization of Thesis

I fully understand the regulations regarding the collection, retention and use of thesis of Southern University of Science and Technology.

1. Submit the electronic version of thesis as required by the University.

2. The University has the right to retain and send the electronic version to other institutions that allow the thesis to be read by the public.

3. The University may save all or part of the thesis in certain databases for retrieval, and may save it with digital, cloud storage or other methods for the purpose of teaching and scientific research. I agree that the full text of the thesis can be viewed online or downloaded within the campus network.

（1）I agree that once submitted, the thesis can be retrieved online and the first 16 pages can be viewed within the campus network.

（2）I agree that ■ upon submission/ □ 12 months after submission, the full text of the thesis can be viewed and downloaded by the public.

4. This authorization applies to decrypted confidential thesis.

Signature of Author: [redacted] Date: 2026.5.25

Signature of Supervisor: [redacted] Date: 2026.5.25

摘 要

在凝聚态物理领域拓扑奇点已成为一个核心焦点。在参数化哈密顿量描述的物质系统中，特征值简并点便会是一个奇点，典型例子包括外尔点、狄拉克点以及节线。这些奇点与拓扑边缘态、手性朗道能级等丰富物理现象直接相关。因此，对拓扑奇点进行数学分类，对于理解拓扑物质相的本质、预测物性具有理论价值。

该领域的理论探索可追溯至 Mermin 运用同伦理论对有序介质中拓扑缺陷的分类工作。Mermin 通过将物理系统描述为从空间到有序参数空间的映射，开创了用代数拓扑研究物理系统的范式。此后，越来越多的拓扑工具被引入能带节点的分类研究中，例如吴泉生等人研究了节线的拓扑分类、非阿贝尔基本群对应非交换的拓扑荷。然而，既有工作大多集中于特定系统的具体计算，尚缺少一个能够统一刻画特征值构型及其特征空间拓扑性质的数学框架。

本文致力于运用代数拓扑方法，建立一套分类参数化二能带三能带厄米和赝厄米哈密顿量中拓扑奇点的理论框架。针对二能带厄米系统与三能带厄米系统，我们可以从丛理论进行分类（对于二能带厄米系统我们还可以从模空间的基本群进行分类），并且提供了球体可视化基本群，加深了对分类的理解。对于二能带赝厄米的情形，可以严格计算讨论清楚。尽管三能带非厄米系统的严格分类尚未最终完成，本文仍从两个角度提供了研究的切入点。其一，针对非厄米系统，其矩阵特征多项式具有对称性，可减少三能带非厄米体系的自由参数数目，从而大幅简化了问题。其二是将相交同调这一拓扑工具引入物理学，提供了参数空间丰富的拓扑信息。我们计算了各种参数化矩阵参数空间（分层奇异空间）的相交同调，获得有趣的结果，并且证明了一个方便计算相交同调的定理，为后续工作开展准备了例子。

本文的核心创新是相交同调的引入，这为处理分层奇异参数空间开辟了新途径。后续的深入工作是计算分层奇异空间的相交同伦，这将能更好的与丛理论适配从而获取特征向量的信息。

关键词：代数拓扑；相交同调；丛理论

ABSTRACT

Topological singularities are a hot topic in modern mathematical physics and condensed matter physics. In a parametrized Hamiltonian matrix, singularities arise where eigenvalues degenerate. These singularities are related to rich physical phenomena, such as topological edge modes and chiral Landau levels. Consequently, classifying topological singularities mathematically will enhance our insight into the nature of topological phases and facilitate the discovery and engineering of novel topological materials.

The problems of topological classification of singularities can be traced back to the pioneering work of Mermin, who applied homotopy theory to classify topological defects in ordered media. By interpreting physical systems as maps from real space into an order-parameter space, Mermin laid the groundwork for applying algebraic topology to physics. Subsequently, topological tools have been increasingly applied to the classification of singularities. For instance, Wu et al. investigated the topological classification of nodal lines in weak spin-orbit coupling systems, where a non-Abelian fundamental group corresponds to non-commutative topological charges. However, the existing research often focuses on specific calculations for particular systems. Hence, we need a unified mathematical framework to consider the topology of eigenvalue configurations and the topological properties of eigenspaces.

This work aims to develop a theoretical framework for classifying topological singularities in parametrized two- and three-band (pseudo) Hamiltonians using methods from algebraic topology. For two- and three-band Hermitian systems, we achieve classification via bundle theory (for two-band systems, we can also classify the fundamental group of the moduli space) and provide a sphere visualization of the fundamental group, thereby deepening understanding of the classification. The two-band pseudo-Hermitian case can be rigorously calculated. Although a strict classification for three-band pseudo-Hermitian systems remains incomplete, we provide two promising methods for investigation. First, we reduce the number of free parameters in three-band pseudo-Hermitian systems using a method based on the translation invariance of the characteristic polynomial, laying a theoretical foundation for future research. Second, we introduce intersection homology, a topological tool, into physics, extracting rich topological information from the parameter space. We compute the intersection homology of various parametrized matrix parame-

ter spaces (stratified singular spaces) and found interesting, meaningful results. We also prove a theorem useful for computing intersection homology. This work provides concrete examples for subsequent work.

Notably, the introduction of intersection homology opens a new avenue for dealing with stratified singular parameter spaces, representing the core innovation of this work. Further work is to compute the intersection homotopy of stratified singular spaces, which could obtain more topological information about eigenvectors by combining with bundle theory.

Keywords: algebraic topology; intersection homology; bundle theory

TABLE OF CONTENTS

LIST OF SYMBOLS AND ACRONYMS

$A(l,s,t)$	Real symmetric 2×2 matrix parameterized by $l,s,t \in \mathbb{R}$
BG	Classifying space of the group G
BZ	Brillouin zone
$B^3(\pi)$	Solid ball of radius π in $\mathbb{R}^3$
$C_*(X)$	Ordinary chain complex of X
C_x, C_y, C_z	Conjugacy classes in quaternion group Q
D_2	Dihedral group with four elements
EG	Universal total space for principal G-bundles
$E(\lambda)$	Eigenspace corresponding to eigenvalue λ
H	Hamiltonian
H_n	n-band Hamiltonian
$H_*(X)$	Ordinary (singular or simplicial) homology of X
$I^{\bar{p}}C_i(X)$	Group of $\bar{p}$-allowable i-chains
$I^{\bar{p}}H_i(X)$	i-th intersection homology group with perversity $\bar{p}$
$\mathrm{O}(1)$	Orthogonal group in one dimension (i.e., $\{+1,-1\}$)
$Prin_G(X)$	Collection of principal G-bundles over space X
Q	Quaternion group
$\mathrm{SO}(2)$	Special orthogonal group in two dimensions
$\mathrm{SO}(3)$	Rotation group in three dimensions
$\mathrm{U}(1)$	Unitary group in one dimension (phase factors)
X_0, X_1, X_2	Strata in parameter space
k	Crystal momentum, $k \in BZ$
t_{ij}	Transition functions between local trivializations U_i and U_j
λ	The eigenvalue of H
$\lambda_{\pm}$	Eigenvalues in a two-band model
$\bar{p}$	Perversity function $\bar{p} : \mathcal{F} \to \mathbb{Z}$
$\bar{p}(S)$	Perversity value assigned to stratum S
$\bar{p}(i)$	Perversity value for strata of formal dimension i
$\mathcal{H}$	Space of three-band Hamiltonians
$I^{\bar{p}}H_*(X)$	PL intersection homology of a PL space X
$\mathcal{M}$	Parameter space or physical space

$\mathcal{S}$	Order parameter space
$\mathbf{r}$	Position vector in $\mathbb{R}^3$
$\phi(\hat{r}, \theta)$	Rotation by angle θ around axis $\hat{r} \in S^2$
$\pi_n(X)$	n-th homotopy group of space X
∂	Boundary operator on chains
$\sim$	Equivalence relation identifying antipodal boundary points
S^n	n-sphere
$S^2/\mathbb{Z}_2$	Quotient space identifying antipodal points
$\mathbb{R}^n$	n-dimensional Euclidean space
$\mathbb{RP}^2$	Real projective plane
$\lvert K \rvert$	Geometric realization of the simplicial complex K

CHAPTER 1 INTRODUCTION

Topological singularities, arising from points with degenerate eigenvalues in a parametrized Hamiltonian H, are fundamental to many areas of modern physics. These singular points, which include well-known examples such as Weyl points, are associated with rich physical phenomena, including topological edge modes and chiral Landau levels. These physical systems can be probed and classified by considering loops in the moduli space of the Hamiltonian, an approach rooted in algebraic topology. The classification of these loops provides insight into the behavior and evolution of eigenvalues and eigenvectors, offering a deeper understanding of the underlying physical systems.

This research seeks to apply algebraic topology, particularly computable invariants, to classify these topological singularities. By focusing on the algebraic and geometric aspects of the problem, we aim to develop a comprehensive framework for understanding the role of topological singularities in various physical contexts.

In Chapter 1, we first introduce some background and Mermin's pioneering work. His work motivates many of our ideas. In Chapter 2 and 3, we research the 2-band and 3-band Hermitian case, respectively. In Chapter 2, we discuss three topological invariants using three different methods and compare them in Section 2.4. In Chapter 3, we present two methods for classifying the 3-band Hermitian Hamiltonian. Both methods are generalizations of the methods in Chapter 2. Then comes the pseudo-Hermitian case. Chapter 4 uses symmetry of the eigen polynomials to reduce the parameters. Then, we use intersection homology to extract topological information of the parameter space of the parametrized matrix in Chapter 5.

1.1 Background

Topological singularities can be understood, from a bird's-eye perspective, as points (or higher-dimensional loci) in parameter space—typically momentum space—where the spectral structure of a system becomes non-regular, such as band degeneracies or gap closings, and around which topological invariants are defined. In Hermitian systems, prototypical examples include Weyl points and Dirac points, which act as effective magnetic monopoles of Berry curvature in momentum space and are characterized by quan-

tized topological charges. These singularities organize global band topology and enforce robust boundary phenomena via bulk-boundary correspondence. From this viewpoint, non-Hermitian singularities such as exceptional points can be seen as natural generalizations in which both eigenvalues and eigenvectors become defective, leading to a richer classification problem that extends the Hermitian paradigm to include spectral winding, nontrivial braiding, and dynamical responses.

There are many types of singularities in non-Hermitian systems. Gain and loss create new types of singularities called exceptional points (EPs). For example, Xue et al. [1] discovered a phenomenon called edge burst. This happens when the imaginary gap closes at a spectral singularity, leading to a transient and highly amplified accumulation of states at the boundary. This effect shows that singular points in non-Hermitian bands can induce dynamic responses that are not seen in standard Hermitian systems. Beyond simple points, non-Hermitian systems have many different types of higher-dimensional singularities. For example, exceptional lines (ELs) are 1D lines where eigenstates coalesce [2]. Similarly, singularity rings (SRs) are 1D rings that provide a richer geometry than isolated points [3]. Exceptional surfaces (ESs) are two-dimensional manifolds in parameter space along which eigenvalues and eigenstates coalesce [4]. In some cases, hypersurface singularities can lead to extended gap-closing regions in parameter space [5]. From a more global perspective, one can use “spectral graphs” to group these singularities based on how their energy branches connect [6].

Topological singularities have potential applications. For example, they are widely applied in topological photonics. As reviewed in [7], singularities like Weyl points and Dirac points can be engineered in photonic crystals and waveguide arrays. These points act as magnetic monopoles and create robust surface states like Fermi arcs. By linking these momentum-space singularities to real-world phenomena, researchers can design new devices for light control and quantized transport.

To describe these systems, researchers need a new toolkit of topological invariants. In Hermitian systems, we mainly look at the properties of eigenstates. However, non-Hermitian topology is much richer because it involves both the winding of eigenvalues and the movement of eigenvectors [8]. There are many tools in mathematics that can help classify topological singularities. Researchers find that these singularities can form complex knots. In these cases, the energy levels wind around each other like a braid. We can use braid groups to label these points [9]. These eigenvalue knots are unique because

they can undergo phase transitions that do not exist in normal systems [10]. In these systems, the energy levels wrap around each other like strings in a braid, forming geometric knots. The way these knots twist is measured by a value called the discriminant invariant [9, 11]. Furthermore, "resultant winding numbers" provide a simple way to classify complex points where many energy bands meet [12–16]. This framework helps us understand how these points double and spread in different dimensions. Other models use Riemann surfaces to describe how multiple singularities work together [17], or show that physical effects like hydrodynamics can create bulk Fermi arcs by pairing different points [18]. Another powerful method is the "singular value decomposition" (SVD). This method is very useful because it provides a framework to restore a generalized bulk-boundary correspondence, which often fails in non-Hermitian systems [19–23]. By using SVD, we can create a new kind of spectrum that treats point gaps and line gaps differently [24]. This ensures that the topology we calculate in the bulk correctly predicts the states we see at the edges.

Homotopy theory in algebraic topology also plays an important role in the classification of topological singularities. The work in [25] studies a three-band model and finds a swallowtail shape that connects nodal lines and exceptional lines. This shows that different types of singularities are not isolated; they are stably connected. To classify these structures, researchers use tools from homotopy theory. For instance, the authors of [26] use homotopy groups to describe nodal lines with PT symmetry. They found that topological charges can be non-Abelian, meaning the lines can braid with each other. Similarly, Wojcik Charles C. et al. uses homotopy to classify gapped phases and define stable topological indices [27].

In our thesis, we focus on many tools in algebraic topology. In addition to homotopy theory, we are also concerned with theories such as bundle theory and intersection homology. In the rest of this section, we briefly review the theory of topological defects established by Mermin in [28], whose pioneering work laid the foundation for utilizing algebraic topology in the classification of topological singularities.

Definition 1.1.1. Let $\mathcal{S}$ be the space of the state at a point, the element in $\mathcal{S}$ is called order parameter and $\mathcal{S}$ is called ordered parameter space. An ordered medium can be described by a map $f : \mathcal{M} \to \mathcal{S}$, where $\mathcal{M}$ is a space.

Example 1.1.2. (Planar spins) Take $\mathcal{M}$ to be a region in $\mathbb{R}^3$, and let $\mathcal{S} = S^1$. Define

$$f : \mathcal{M} \to S^1, \qquad f(\mathbf{r}) = e^{i\phi(\mathbf{r})},$$

where $\phi : \mathbb{R}^3 \to [0, 2\pi)$. This assigns to each point of $\mathcal{M}$ a unit vector in the plane.

Example 1.1.3. (Ordinary spins) Let $\mathcal{M}$ be a region in $\mathbb{R}^3$, and let $\mathcal{S} = S^2$, the 2-sphere. Let $f : \mathcal{M} \to S^2$. This assigns to each point of $\mathcal{M}$ a unit vector in $\mathbb{R}^3$.

Example 1.1.4. (Biaxial nematics) Take $\mathcal{M}$ be a region in $\mathbb{R}^3$. Take

$$\mathcal{S} = \{\text{rectangular box with fixed size centered at origin in } \mathbb{R}^3\} = \mathrm{SO}(3)/\mathrm{D}_2.$$

So an order medium meets above requirements is a space $\mathcal{M}$ with a map $f : \mathcal{M} \to \mathcal{S}$.

Example 1.1.5. (Dipole-locked A phase of superfluid helium-3) Take $\mathcal{M}$ be a region in $\mathbb{R}^3$. Take $\mathcal{S} = \{\text{distinguished orthonormal axes}\}$. Since distinguished orthonormal axes can be viewed as two orthonormal sticks, $\mathcal{S} = \mathrm{SO}(3)$.

Next, we consider the special case of Brillouin zone BZ. Let $H : BZ \to \mathcal{S}$ be a map assigning each $k \in BZ$ to a Hamiltonian. Let $\iota : S^p \to BZ$ be a null homotopic embedding. Then

$$[H \circ \iota] \in \pi_p(\mathcal{S}).$$

If $\iota(S^p)$ encloses a node in the space $\mathcal{S}$, $\iota(S^p)$ cannot contract to a point, and thus

$$[H \circ \iota] \neq 0.$$

Definition 1.1.6. We call $[H \circ \iota] \in \pi_p(\mathcal{S})$ a topological charge of the node.

Example 1.1.7. (Planar spins) $\pi_1(S_1) = \mathbb{Z}$, the group elements are called winding number.

Example 1.1.8. (Ordinary spins) Take $\mathcal{M}$ be a region in $\mathbb{R}^3$. Take $\mathcal{S} = S^2$. Since all loops on S^2 can be shrunk to a constant loop, we have $\pi_1(S^2) = 0$.

To figure out the case in biaxial nematics, we need the following useful fact. A detailed proof can be seen in [26].

Example 1.1.9. (Biaxial nematics) The fundamental group of $\mathrm{SO}(3)/\mathrm{D}_2$ is

$$\pi_1\big(\mathrm{SO}(3)/\mathrm{D}_2\big) = \pi_1\big(\mathrm{SU}(2)/\overline{\mathrm{D}_2}\big) = \pi_0\big(\overline{\mathrm{D}_2}\big) = \pi_0(\mathrm{Q}) = \mathrm{Q}.$$

Example 1.1.10. (Dipole-locked A phase of superfluid helium-3) The fundamental group of $\mathrm{SO}(3)$ is

$$\pi_1\big(\mathrm{SO}(3)\big) = \pi_1\big(\mathbb{RP}_3\big) = \pi_1\big(S^3/\mathbb{Z}_2\big) = \mathbb{Z}_2.$$

When the space is not based, we consider the free homotopy equivalence between maps, and then the homotopy group is classified by free homotopy.

Theorem 1.1.11. Let X be a space. Let f based at x, g based at y be two representation

elements of $\pi_1(X)$. Then $f \simeq g$ by free homotopy precisely when one can find a path isomorphism c taking $[f] \in \pi_1(X, x)$ to $[g] \in \pi_1(X, y)$.

Since fusion of nodes corresponds to charge multiplication, it is determined by the multiplication rule of the conjugacy class.

Example 1.1.12. The quaternion group Q has following conjugate class:

$$C_0 := \{1\}, \quad \overline{C_0} := -1, \quad C_x := \{\pm i\sigma_x\}, \quad C_y := \{\pm i\sigma_y\}, \quad C_z := \{\pm i\sigma_z\},$$

where σ_x, σ_y, σ_z are Pauli matrices. The multiplication table [28] are as follows:

$\times$	C_0	$\overline{C_0}$	C_x	C_y	C_z
C_0	C_0	$\overline{C_0}$	C_x	C_y	C_z
$\overline{C_0}$	$\overline{C_0}$	C_0	C_x	C_y	C_z
C_x	C_x	C_x	$2C_0 + 2\overline{C_0}$	$2C_z$	$2C_y$
C_y	C_y	C_y	$2C_z$	$2C_0 + 2\overline{C_0}$	$2C_x$
C_z	C_z	C_z	$2C_y$	$2C_x$	$2C_0 + 2\overline{C_0}$

Figure 1-1 Multiplication table of the conjugacy classes of Q

From the table, we observe that most results consist of a unique conjugate group, except for some cases where the result is an addition of two conjugate classes. That means the result is not unique when we do multiplication.

Note that the multiplication of two defects is a path connecting two defects, and let the two defects fuse to another defect along this path. The non-unique result is rooted in the non-unique way of this path passing through other defects.

Example 1.1.13. Since

$$-(i\sigma_x) = (i\sigma_y)(i\sigma_x)(i\sigma_y)^{-1},$$

the x defect can converted to its antidefect by passing through y defects. Hence, there are two ways to multiply two x defects to obtain different results: the first is to multiply them trivially; we obtain a nontrivial defect. The second is to multiply them by passing through y defects; we obtain a trivial defect.

We stop the introduction to Mermin's study here. Mermin's work introduces homotopy theory into the classification of nodes in bands, and later, more and more topological tools are applied in this problem [26, 27, 29–31].

Mermin's work studies the topology of an ordered medium. In this article, we'll focus on the topology of the configuration of eigenvectors and eigenvalues of parametrized Hamiltonians.

1.2 Topology of energy bands

The topology of energy bands is the topology of the configuration of eigenvalues and eigenspaces.

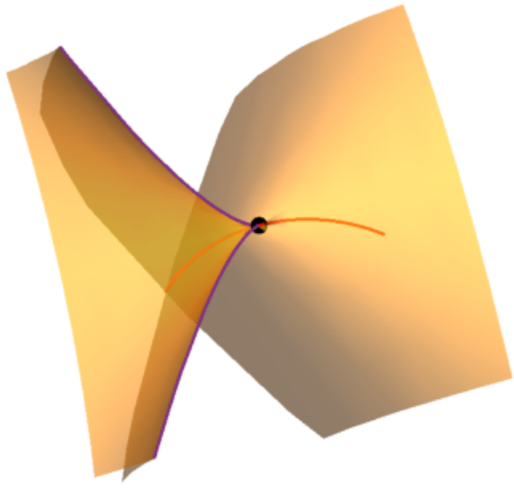

Figure 1-2 This is the swallowtail space in the parameter space, at which the eigenpolynomial of matrix in (1-1) is zero.

Example 1.2.1. Consider the matrix

$$H = \begin{bmatrix} g_3 & g_2 \\ -g_2 & -g_3 \end{bmatrix}, \quad g_2, g_3 \in \mathbb{R}.$$

We divided the g_3-g_2 plane into three regions: Let

$$X_0 := \{(0,0)\}, \quad X_1 := \{(g_3, g_3), (g_3, -g_3) \mid g_3 \in \mathbb{R}\}, \quad X_2 := \mathbb{R}^2.$$

Let $\lambda_{\pm}$ be two eigenvalues and $E(\lambda)$ be the eigenspace. In X_0, the dimension of eigenspace is 2 and

$$\lambda_+ = \lambda_- =: \lambda.$$

In $X_1 - X_0$, the dimension of eigenspace is 1 and

$$\lambda_+ = \lambda_- =: \lambda.$$

In $X_2 - X_1$, the dimension of eigenspace is 1 and $\lambda_+ \neq \lambda_-$.

It's a stratified space with each stratum characterizing different behavior of eigenvalues and eigenvectors.

Definition 1.2.2. If a point in parameterized space does not have n distinct eigenvalues,

we say it is a singular point.

Example 1.2.3. (The swallowtail) Consider the parametrized matrix

$$H = \begin{bmatrix} -g_1 - g_2 + 1 & -g_1 & -g_2 \\ g_1 & g_1 + g_3 & -g_3 \\ g_2 & -g_3 & g_2 + g_3 \end{bmatrix}, \quad g_1, g_2, g_3 \in \mathbb{R}. \tag{1-1}$$

The singular points locally look like a swallowtail, see Figure 1-2. The swallowtail has four singular lines, and one of them is an isolated singular line; there is one singular point (meeting point) at the origin. Similarly to the previous example, the swallowtail is also a stratified space, see [29].

CHAPTER 2 2-BAND HERMITIAN HAMILTONIANS OVER ℝ

In this section we only consider Hermitian Hamiltonian over ℝ. 2-band Hermitian Hamiltonian over ℝ is the most simple examples which is also significant. The following ways we only consider loops in gapped region to detect singular points. In this section we provide several ways of classifying singular points by considering loops not intersecting with singular points.

2.1 Classifying I: Hopf bundles over ℝ

This section will first review discussion in Section 5.1 in [32], and then apply it to our problem.

Let $Prin_G(S^n)$ be a collection of all principal G-bundles over S^n. Since

$$Prin_G(S^n) \simeq \pi_{n-1}(G),$$

we have

$$Prin_{S^0}(S^1) \simeq \pi_0(S^0) = \{\pm 1\}.$$

So there are only two principal S^0-bundles over S^1 (up to isomorphism). More precisely, the two principal S^0-bundles over S^1 are trivial bundles and Hopf bundles. The trivial bundle is

$$S^0 \to S^1 \times S^0 \to S^1$$

whose total space is disconnected. The Hopf bundle, whose total space is connected, is

$$S^0 \to S^1 \xrightarrow{h} S^1,$$

where

$$h : S^1 \to S^1, \quad (x_1, x_2) \mapsto (2x_1x_2, x_1^2 - x_2^2).$$

Hence, show that a principal S^0-bundle over S^1 a Hopf bundle is equivalent to show that the total space is connected.

Proposition 2.1.1 (Proposition 4.2 in [32])**.** Suppose that M is a smooth manifold, $H(p)$ is a complex Hermitian $n \times n$ matrix depending smoothly on the parameter $p \in M$, and

$U \subset M$ is an open subset such that the eigenspace corresponding to the k-th eigenvalue is one-dimensional on U. Then one can define a principal $\mathrm{U}(1)$-bundle (or an S^0-bundle) consisting of normalized eigenvectors corresponding to the k-th eigenvalue of $H(p)$ for all $p \in U$.

Remark 2.1.2. Let ψ be a physical state, then ψ and $\lambda\psi$, $\forall\lambda \in \mathrm{U}(1)$ corresponding to the same state. This physical meaning motivates the existence of $\mathrm{U}(1)$-bundle in above theorem.

Every symmetric real 2×2 matrices is of the form

$$A\,(l,s,t) = \begin{bmatrix} l+t & s \\ s & l-t \end{bmatrix},$$

which has eigenvalues $\lambda_{\pm} = l \pm \sqrt{t^2+s^2}$. Consider the eigenbundle corresponding to eigenvalue λ_+. There is no global representation of normalized eigenvector of λ_+, so we define two open sets: let

$$U_1 := \mathbb{R}^2 - \{(0,t)|t \leqslant 0\} \text{ and } U_2 := \mathbb{R}^2 - \{(0,t)|t \geqslant 0\}.$$

In U_1, the normalized eigenvector of λ_+ is

$$v_1\,(l,s,t) = \frac{1}{\sqrt{2\,(s^2+t^2)+2t\sqrt{t^2+s^2}}}\begin{pmatrix} t+\sqrt{s^2+t^2} \\ s \end{pmatrix},$$

and in U_2, the normalized eigenvector corresponding to λ_+ is

$$v_2\,(l,s,t) = \frac{1}{\sqrt{2\,(s^2+t^2)-2t\sqrt{t^2+s^2}}}\begin{pmatrix} s \\ -t+\sqrt{s^2+t^2} \end{pmatrix}.$$

We observe that $v_i(l,s,t)$ is independent of l and only depends on s/t, $i = 1,2$.

Example 2.1.3. On the line $s = 2t$, we have

$$\phi_- = \begin{bmatrix} \frac{1-\sqrt{5}}{2} \\ 1 \end{bmatrix}, \phi_+ = \begin{bmatrix} \frac{1+\sqrt{5}}{2} \\ 1 \end{bmatrix}, t > 0,$$

$$\phi_- = \begin{bmatrix} \frac{1+\sqrt{5}}{2} \\ 1 \end{bmatrix}, \phi_+ = \begin{bmatrix} \frac{1-\sqrt{5}}{2} \\ 1 \end{bmatrix}, t < 0,$$

Therefore, there is a change of base space

$$\text{The base space } \mathbb{R}^3 - 0 \xrightarrow{\text{can change to}} \mathbb{R} \times \mathbb{R}_{>0} \times S^1$$

The "coordinate" l and r is redundancy, so the eigenbundle is of the form:

$$\pi_0 : \mathbb{R} \times \mathbb{R}_{>0} \times E \to \mathbb{R} \times \mathbb{R}_{>0} \times S^1, \quad (l, r, x) \mapsto (l, r, \pi(x)),$$

where $\pi : E \to S^1$ is a S^0-bundle over S^1. In the following, we only focus on S^0-bundle $\pi : E \to S^1$.

$\mathbb{R}^3 \to \mathbb{R} \times \mathbb{R} \times S^1$
$(l, s, t) \mapsto (l, r, x)$

l: same l in (l, s, t)
r: strech $r > 0$ times
x: a point x in S^1

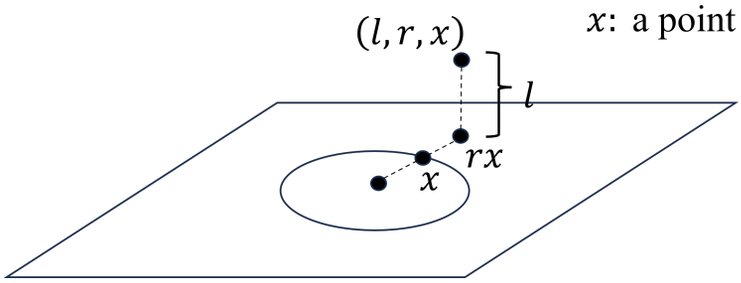

Figure 2-1 The coordinate system (l, r, x) on $\mathbb{R}^3 \setminus \{0\}$. Here, l, r, and x denote the geometric quantities indicated in the figure, providing an alternative parametrization of points in $\mathbb{R}^3 \setminus \{0\}$ besides the standard Cartesian coordinates.

Proposition 2.1.4. v_1 defines a local section of E over S^1.

Proof. We want to show $\pi v_1|_{S^1} = id$, i.e., $\pi v_1(x) = x$, $\forall x \in S^1$. It suffices to show $v_1(x) \in \pi^{-1}(x)$. Since $\pi^{-1}(x)$ is the fiber, and $v_1(x)$ is the first eigenvector at x, we have $v_1(x) \in \pi^{-1}(x)$ by construction of eigenbundle.

Recall that

$$v_i(l, s, t) = v_j(l, s, t) t_{ji}(l, s, t), i, j = 1, 2,$$

where t_{12} and t_{21} are transition functions defined on $U_1 \cap U_2 = \mathbb{R}^2 - \{(0, t) | t \in \mathbb{R}\}$. Since eigenvectors only depends on s/t, it suffices to consider them on the circle

$$s^2 + t^2 = 1.$$

$$v_1(l, s, t) = \frac{1}{\sqrt{(t+1)^2 + s^2}} \begin{bmatrix} t+1 \\ s \end{bmatrix} = \frac{1}{\sqrt{s^2(t+1)^2 + s^4}} \begin{bmatrix} |s|(t+1) \\ s^2 \end{bmatrix},$$

and

$$v_2(l, s, t) = \frac{1}{\sqrt{(-t+1)^2 + s^2}} \begin{bmatrix} s \\ -t+1 \end{bmatrix}$$

$$= \frac{1}{\sqrt{s^2(t+1)^2 + (1-t^2)^2}} \begin{bmatrix} s(t+1) \\ 1-t^2 \end{bmatrix}$$

$$= \frac{1}{\sqrt{s^2(t+1)^2 + s^4}} \begin{bmatrix} s(t+1) \\ s^2 \end{bmatrix}.$$

Hence,

$$t_{12}(s,t) = t_{21}(s,t) = \begin{cases} 1, & s > 0 \\ -1, & s < 0 \end{cases}.$$

Proposition 2.1.5. The total space is connected, and thus the bundle is isomorphic to the Hopf bundle.

Proof. By Property 2.23 in [33]: If $\mathcal{U}$ is a connected covering of a topological space X and X has a subset A with $A \cup U_i \neq \emptyset$ for any $U_i \in \mathcal{U}$, then X is connected.

Denote $V_1 = S^1 - \{(0,-1)\}$ and $V_2 = S^1 - \{(0,+1)\}$. Note that

$$v_1|_{V_1} : V_1 \to v_1(V_1)$$

and

$$\pi|_{v_1(V_1)} : v_1(V_1) \to V_1$$

are inverse, because v_1 are local sections of E over S^1(meaning that v_1 is injective). So as $v_2|_{V_2}$ and $\pi|_{v_2(V_2)}$. π^{-1} is continuous and $\pi^{-1}(V_i)$ is connected, so $\{\pi^{-1}(V_i)\}$ is a connected covering of E. Then we have

$$\pi^{-1}(V_1) \cup \pi^{-1}(V_2) = \pi^{-1}(S^1) = E.$$

Let

$$H = \{(s,t) | s > 0\} \subset V_1 \cap V_2$$

be a connected subset. We've proved $v_i t_{ij} = v_j$ and $t_{ij} = 1$ for $s > 0$. So $v_1(H)$ is equal to $v_2(H)$ and we denote them as $v(H)$. $v(H) \cap \pi^{-1}(V_i) \neq \emptyset$, $i = 1,2$. Using the property above, E is connected. Thus E is a Hopf bundle.

Theorem 2.1.6. Let

$$A(l,s,t) = \begin{bmatrix} l+t & s \\ s & l-t \end{bmatrix},$$

which has eigenvalues $\lambda_\pm = l \pm \sqrt{t^2 + s^2}$ be a symmetric real matrix where $(l,s,t) \in \mathbb{R}^3$. Then there is a S^0-bundle over $\mathbb{R}^3 - \{(l,0,0) | l \in \mathbb{R}\}$ with fiber being the eigenspace

corresponding to λ_+. Then this bundle over any loops enclose $\hat{l}$-axis is a Hopf bundle while over the loop not enclose $\hat{l}$-axis is a trivial bundle, see Figure 2-2.

Replacing first eigenvalues tosecond eigenvalues, the statement is also true.

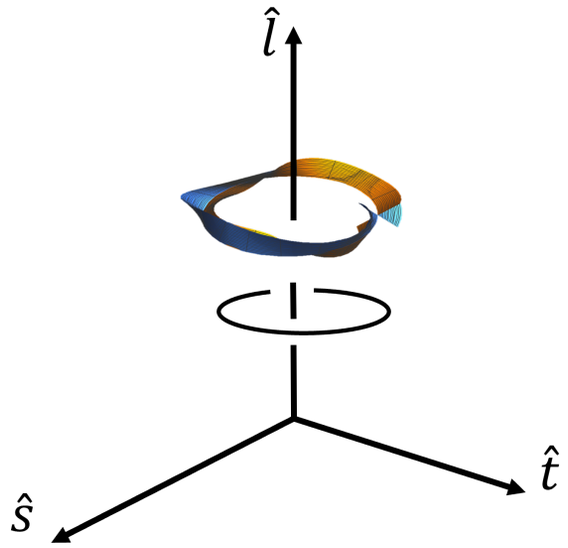

Figure 2-2 A loop in the parameter space l-s-t enclosing the $\hat{l}$-axis. The two eigenvectors along the loop each form a Hopf bundle, represented in blue and yellow respectively.

It leads to that the eigenvector of first (resp. second) eigenvector changes sign after the parameter evolves along the whole round of the loop enclosing $\hat{l}$-axis. A summary is in T able2-1.

Loop	Encloses $\hat{l}$	Not encloses $\hat{l}$
Eigenbundle of the first/second eigenvector	Hopf	trivial
State of first/second eigenvector after rotation around the loop	changes sign	initial

Table 2-1 Classification of loops around the degeneracy axis.

We compare our construction with the Berry-phase formulation. Following the approach in [34], we recall that if an electron's spin is guided adiabatically along an arbitrary closed loop by a magnetic field, the resulting change in the geometric phase is equal to minus one-half of the solid angle Ω subtended by the area swept out by the tip of the magnetic field vector. Specifically, for a system described by the parameterized Hamiltonian:

$$H(\theta,\phi) = \frac{\hbar}{2}\begin{pmatrix} \cos\theta & \sin\theta e^{-i\phi} \\ \sin\theta e^{i\phi} & -\cos\theta \end{pmatrix},$$

the Berry phase is given by $\gamma = -\frac{1}{2}\Omega$.

In this thesis, we utilize the matrix representation:

$$A(l,s,t)=\begin{bmatrix} l+t & s \\ s & l-t \end{bmatrix}.$$

By mapping the parameters as follows:

$$\begin{cases} l+t=\cos\theta \\ l-t=-\cos\theta \\ s=\sin\theta e^{i\phi} \\ \phi=0 \end{cases} \Longrightarrow \begin{cases} l=0 \\ t=\cos\theta \\ s=\sin\theta \end{cases}.$$

The following three cases provide evidence that our topological classification aligns with this physical description:

The first case is the parameter θ ranges from 0 to 2π. The corresponding solid angle is $\Omega=2\pi$, which yields a nontrivial Berry phase $\gamma=-\frac{1}{2}(2\pi)=-\pi$. In the l-s-t space, the trajectory is a loop $[0,2\pi]\to\mathbb{R}^3$ defined by $\theta\mapsto(0,\sin\theta,\cos\theta)$. This loop encloses the $\hat{l}$-axis, characterizing a nontrivial bundle (Hopf bundle). This topological result is consistent with the nontrivial Berry phase.

The second case is the parameter θ ranges from 0 to π and then returns to 0. The resulting solid angle is $\Omega=0$, leading to a trivial Berry phase $\gamma=0$. The corresponding path in l-s-t space is a semi-circle from $(0,0,1)$ to $(0,0,-1)$ that is retraced. Since this loop does not enclose the $\hat{l}$-axis, it corresponds to a trivial bundle, matching the physical prediction.

The third case is the parameter θ ranges from 0 to 4π. The solid angle is $\Omega=4\pi$, giving a Berry phase of $\gamma=-2\pi$. Physically, this is trivial as the phase factor $e^{-i2\pi}=1$ leaves the state ψ invariant. In l-s-t space, the loop encircles the $\hat{l}$-axis twice. This configuration represents a direct sum of two Hopf bundles, which is topologically trivial in this context, aligning with the trivial Berry phase.

2.2 Classifying II: Fundamental group of moduli space

In classifying I, we consider two eigenvectors separately, which is useful when two eigenvectors have high symmetry. In this section, we provide the second classification considering two eigenvectors simultaneously.

In order to more clearly represent the underlying physical meaning, we introduce a different notation from that employed in the previous section. We denote eigenvetor asso-

ciated to eigenvalue $\omega_{\pm}$ by $\phi_{\pm}$. Recall any Hermitian 2×2 matrix H can be represented by Pauli matrix:

$$\sigma_1 = \begin{bmatrix} 0 & 1 \\ 1 & 0 \end{bmatrix}, \quad \sigma_2 = \begin{bmatrix} 0 & -i \\ i & 0 \end{bmatrix}, \quad \sigma_3 = \begin{bmatrix} 1 & 0 \\ 0 & -1 \end{bmatrix},$$

i.e., $H_2 = f_0 I + f_1\sigma_1 + f_2\sigma_2 + f_3\sigma_3$. With PT-symmetry (to make H_2 real), $f_2 = 0$. So the Hamiltonian takes the form

$$H_2 = \begin{bmatrix} f_0 + f_3 & f_1 \\ f_1 & f_0 - f_3 \end{bmatrix}.$$

Its eigenvalues and eigenvectors are:

$$(f_1 \neq 0)\ \omega_- = f_0 - \sqrt{{f_1}^2 + {f_3}^2}, \quad \omega_+ = f_0 + \sqrt{{f_1}^2 + {f_3}^2},$$

$$\phi_- = \begin{bmatrix} -\frac{-f_3 + \sqrt{{f_1}^2 + {f_3}^2}}{f_1} \\ 1 \end{bmatrix}, \quad \phi_+ = \begin{bmatrix} -\frac{-f_3 - \sqrt{{f_1}^2 + {f_3}^2}}{f_1} \\ 1 \end{bmatrix},$$

$$(f_1 = 0, f_3 < 0)\ \omega_- = f_0 - |f_3|, \quad \omega_+ = f_0 + |f_3|,$$

$$\phi_- = \begin{bmatrix} 1 \\ 0 \end{bmatrix}, \quad \phi_+ = \begin{bmatrix} 0 \\ 1 \end{bmatrix},$$

$$(f_1 = 0, f_3 > 0)\ \omega_- = f_0 - |f_3|, \quad \omega_+ = f_0 + |f_3|,$$

$$\phi_- = \begin{bmatrix} 0 \\ 1 \end{bmatrix}, \quad \phi_+ = \begin{bmatrix} 1 \\ 0 \end{bmatrix}.$$

Since eigenvectors are independent on f_0, so we assume $f_0 = 0$. We first depict eigenspace spanned by ϕ_-(blue) and ϕ_+(red) in Figure 2-3, where the short sticks denotes 1-dimensional eigenspaces.

We have the following observation: Firstly, along the line $f_1 = kf_3$, the system has same eigenvectors. Secondly, this field is a good example for a system that should rotate 4π to return to initial, see Figure 2-4; the blue round is rotating 2π, turning the vector to its inverse; the red round is the second round of rotating 2π, turning the vector to its initial. Thirdly, this leads to an interesting phenomenon: eigenvectors swapping. Since rotating π along the loop corresponding to rotating $\pi/2$ of eigenvectors and the angle between $\phi_{\pm}$ is $\pi/2$, we have the swapping of ϕ_+ and ϕ_- when we "passing through" the origin. See

Figure 2-5. Here, the "swap" means the first eigenvector becomes the second eigenvector and the second eigenvector becomes the first eigenvector.

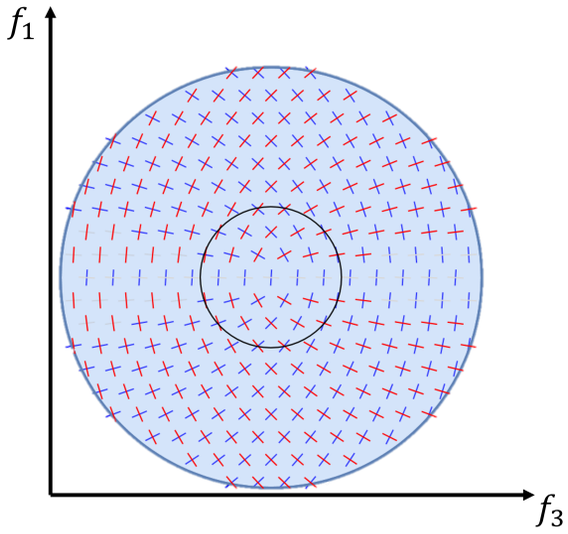

Figure 2-3 The eigenvector field over the parameter space f_1-f_3. To each point in parameter space, we assign two 1-dimensional eigenspaces of the parametrized matrix, depicted in blue ϕ_- and red ϕ_+.

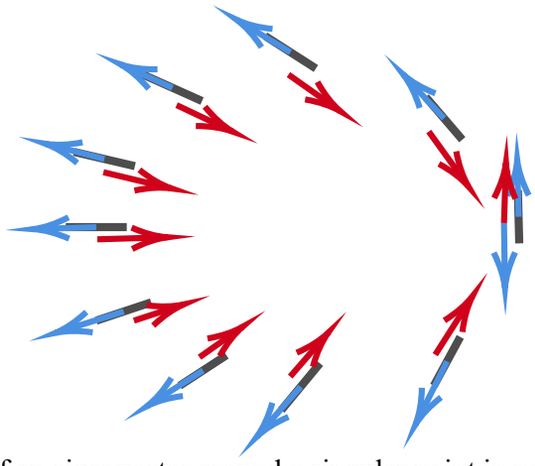

Figure 2-4 Evolution of an eigenvector around a singular point in parameter space. After one revolution, the eigenvector changes sign and does not return to its initial state. A second revolution is required to recover the original eigenvector. The blue and red arrows represent the first and second revolutions, respectively.

The eigenvalues do not matter; the order of corresponding eigenvectors matters. So we focus on the ordered pair (ϕ_-, ϕ_+). The moduli space is $M_2 := \{(f_3, f_1) \in \mathbb{R}^2\}/\sim$, where the relation $\sim$ is

$$(f_3, f_1) \sim (f_3', f_1') \iff H_2(f_3, f_1) \text{ and } H_2(f_3', f_1') \text{ have same ordered pair } (\phi_-, \phi_+).$$

We can reduce the problem to study the topology of M_2.

Proposition 2.2.1. $M_2 \simeq S^1$.

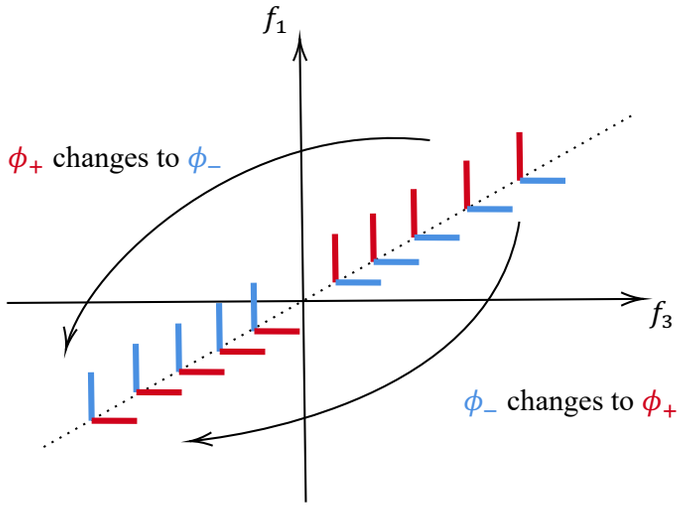

Figure 2-5 Exchange of eigenvectors across the degeneracy point. As the parameter passes through the origin in the f_1-f_3 plane, the eigenvector ϕ_+ continuously changes into ϕ_-, while ϕ_- changes into ϕ_+.

Proof. From observation we have (ϕ_-, ϕ_+) coincides on the line. Hence, we only need to consider H_2 on the unit sphere S^1 in $\mathbb{R}^2$. The following will shows on each point in S^1 we have different (ϕ_-, ϕ_+). On S^1, let $f_3 = cos\theta$, $f_1 = sin\theta$. The eigenvalues and normalized eigenvectors corresponding to θ are as following:

$$\omega_- = -1, \quad \omega_+ = 1,$$

$$\phi_- = \begin{bmatrix} -\sin(\theta/2) \\ \cos(\theta/2) \end{bmatrix}, \quad \phi_+ = \begin{bmatrix} \cos(\theta/2) \\ \sin(\theta/2) \end{bmatrix}.$$

We claim that $\{H_2(f_3, f_1) \mid (f_3, f_1) \in S^1\} \xrightarrow{1:1} \overline{(f_3, f_1)} \in M_2$. Indeed, there are two ways to show it.

The first way is to considering $H_2(\phi_-)$. H_2 can be represented by ϕ_-:

$$H_2 = \begin{bmatrix} f_3 & f_1 \\ f_1 & -f_3 \end{bmatrix} = \begin{bmatrix} \cos\theta & \sin\theta \\ \sin\theta & -\cos\theta \end{bmatrix} = 1 - 2\phi_-{\phi_-}^T,$$

$$\phi_- \in SO(2) \xrightarrow{2:1} H_2(\phi_-) = 1 - 2\phi_-{\phi_-}^T,$$

since $H_2(\phi_-) = H_2(-\phi_-)$. Hence, $M_2 = \mathrm{SO}(2)/\mathbb{Z}_2 = S^1/\mathbb{Z}_2 = S^1$.

The second way is to considering θ:

$$e^{i\theta} \in S^1 \xrightarrow{1:1} \begin{bmatrix} \cos\theta & -\sin\theta \\ \sin\theta & \cos\theta \end{bmatrix} \in SO(2) \xrightarrow{1:1} \theta \in [0, 2\pi) \xrightarrow{1:1} H_2(\theta) = \begin{bmatrix} \cos\theta & \sin\theta \\ \sin\theta & -\cos\theta \end{bmatrix}.$$

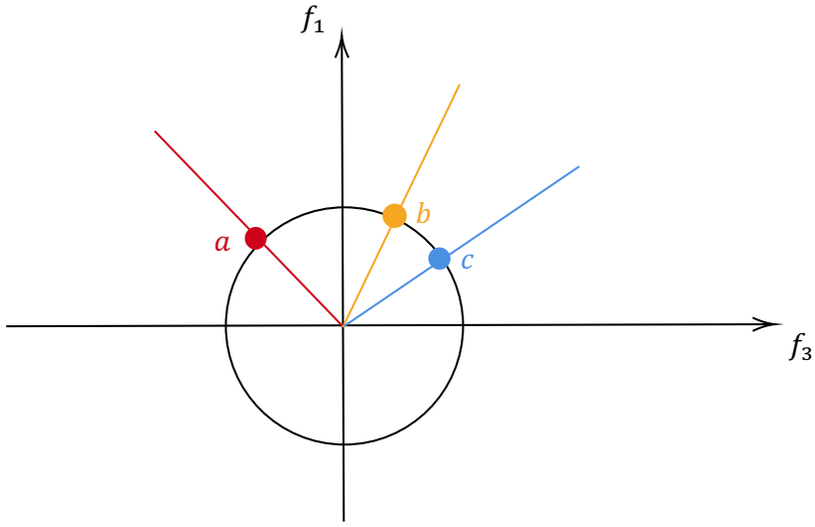

Figure 2-6 Points lying on the same line through the origin determine the same eigenvector. Hence eigenvectors are parametrized by directions, represented by points on S^1.

The geometric view is as following: Each point in S^1 repesents an equivalence class in M_2. For example, a (resp. b,c) represents points (f_3, f_1) on the red (resp. yellow, blue) line (See Figure 2-6). Hence, $\pi_1(M_2) = \pi_1(S^1) = \mathbb{Z}$.

2.3 Classifying III: $\pi_1(\mathrm{SO}(2)/\mathrm{O}(1))$

A two band Hamiltonian is

$$H_2 = \sum_{j=1}^{2} j \left|u_k^j\right\rangle \left\langle u_k^j\right|,$$

where $\left|u_k^j\right\rangle$ are eigenvectors by spectrum theorem. The Hamiltonian H_2 can be determined by a set of "right hand" orthonormal vectors $\left|u_k^j\right\rangle$ and unchanged for two of eigenvectors flip:

$$\left|u_k^j\right\rangle \mapsto -\left|u_k^j\right\rangle.$$

Note that H_2 remains unchanged for two eigenvectors flip, not one of them. This is because we require all eigenvectors to form a right-hand frame (Any odd number flip will

change the determinant from 1 to -1). Therefore, H_2 can be describe by

$$\mathrm{SO}(2)/\mathrm{O}(1) = S^1/\mathbb{Z}_2 = \mathbb{RP}^1.$$

Then $\pi_1\big(\mathrm{SO}(2)/\mathrm{O}(1)\big) = \mathbb{Z}_2$ characterize all nontrivial loops in this parametrized system.

The visualizing of $\pi_1\big(\mathrm{SO}(2)/\mathrm{O}(1)\big) = \mathbb{Z}_2$ is as following: $\mathrm{SO}(2)/\mathrm{O}(1)$ is S^1 identifying antipodal points. The generator of $\pi_1\big(\mathrm{SO}(2)/\mathrm{O}(1)\big) = \mathbb{Z}_2$ is depicted in Figure 2-7.

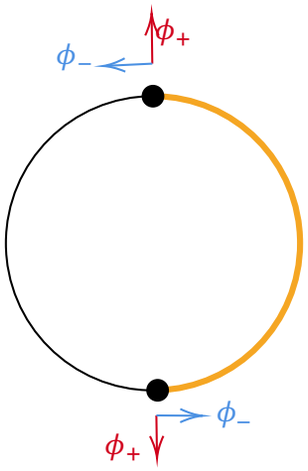

Figure 2-7 A generator of $\pi_1\big(\mathrm{SO}(2)/\mathrm{O}(1)\big)$, represented as a nontrivial loop in $S^1/\mathbb{Z}_2$. Each point on the loop corresponds to an eigenframe, and traversing the loop describes the continuous rotation of the eigenframe. The eigenframes at the two ends of the loop are illustrated above.

Along this loop, the eigenvectors evolves to their inverse.

2.4 Comparison of 3 classifying methods

Topological invariants obtained by classification I, II, and III have different meanings.

In classification I the two eigenvectors are orthogonal, so we only consider one eigenspace. We identify an normalized eigenvector with its inverse, since we use the language of bundle and the fiber of the bundle is an eigenspace. In classification II, we distinguish an eigenvector with its inverse. In classification III, the two eigenvectrs form a right-hand frame, so we can only consider one eigenvector. Quotient $\mathrm{O}(1)$ means we identify an normalized eigenvector with its inverse.

We can choose different topological invariants in different cases by physical meaning.

CHAPTER 3 3-BAND HERMITIAN HAMILTONIAN OVER ℝ

A three band Hamiltonian is

$$H_k = \sum_{j=1}^{3} j \left|u_k^j\right\rangle \left\langle u_k^j\right|.$$

The Hamiltonian H_k can be determined by a set of "right hand" orthonormal vectors $\left|u_k^j\right\rangle$ and unchanged for two of eigenvectors flip. The Hamiltonian H_k remains unchanged for two of the eigenvectors flip, not one or three of them, because we need all eigenvectors to form a right-hand frame (Any odd number flips will change the determinant from 1 to -1). The Hamiltonian H_k can be describe by $\mathrm{SO}(3)/\mathrm{D}_2$. It's some kind of eigenbundle of H_k, see Figure 3-1.

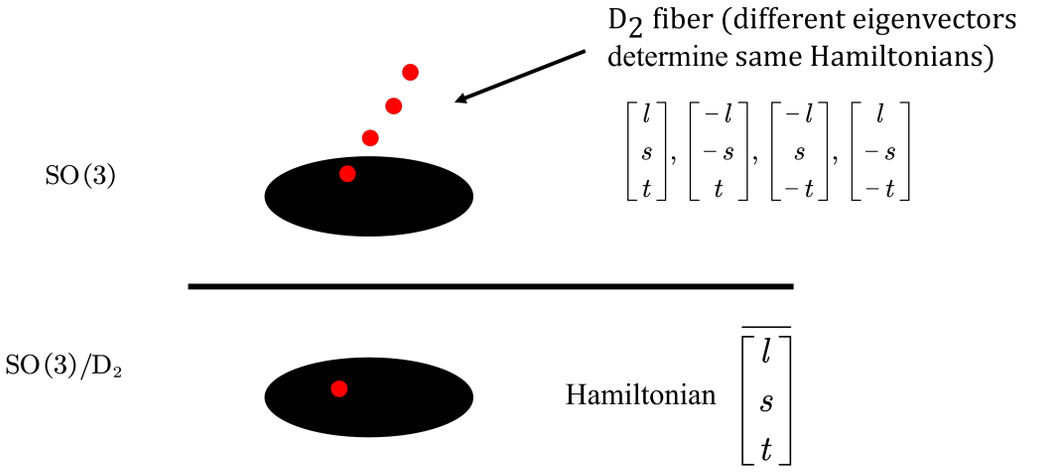

Figure 3-1 The D_2 fiber bundle structure for a 3-band Hamiltonian. Each fiber consists of four eigenframes, each formed by three mutually orthogonal eigenvectors. All four points in the fiber correspond to the same Hamiltonian.

3.1 Classifying I: Universal bundles of $\mathrm{D}_2 \to \mathrm{SO}(3) \to \mathrm{SO}(3)/\mathrm{D}_2$

Consider the bundle

$$\mathrm{D}_2 \hookrightarrow \mathrm{SO}(3) \xrightarrow{\pi} \mathrm{SO}(3)/\mathrm{D}_2 =: X, \quad \pi(x) = \bar{x}.$$

The isomorphism classes of principal D_2-bundles over X are denoted by $Prin_{\mathrm{D}_2}(X)$

and

$$Prin_{\mathrm{D}_2}(X) \simeq [X, B\mathrm{D}_2],$$

where $B\mathrm{D}_2$ is the classifying space of D_2. The following will show which $\phi \in [X, B\mathrm{D}_2]$ corresponds to the principal D_2-bundle we considered.

The classifying bundle of $\mathrm{O}(1)$ is

$$f : E\mathrm{O}(1) = V_1(\mathbb{R}^\infty) \to Gr_1(\mathbb{R}^\infty), \quad f(v) = \mathrm{span}(v).$$

Then the classifying bundle of

$$\mathrm{D}_2 \simeq \mathbb{Z}_2 \times \mathbb{Z}_2 = \mathrm{O}(1) \times \mathrm{O}(1)$$

is the product of two morphisms

$$f \times f : V_1(\mathbb{R}^\infty) \times V_1(\mathbb{R}^\infty) \to Gr_1(\mathbb{R}^\infty) \times Gr_1(\mathbb{R}^\infty).$$

Remark 3.1.1. $V_1(\mathbb{R}^\infty)$ is the Stiefel manifold. $V_k(\mathbb{R}^n)$ is the set of all orthonormal k-frames in $\mathbb{R}^n$.

We need to find

$$\phi : X \to Gr_1(\mathbb{R}^\infty) \times Gr_1(\mathbb{R}^\infty),$$

such that $\pi : \mathrm{SO}(3) \to X$ appears in the pullback of ϕ and $f \times f$:

$$\begin{array}{ccc} \mathrm{SO}(3) & \longrightarrow & V_1(\mathbb{R}^\infty) \times V_1(\mathbb{R}^\infty) = E\mathrm{D}_2 \\ \downarrow{\scriptstyle \pi} & & \downarrow{\scriptstyle f\times f} \\ X & \xrightarrow[\phi]{} & Gr_1(\mathbb{R}^\infty) \times Gr_1(\mathbb{R}^\infty) = B\mathrm{D}_2 \end{array}$$

where $f : V_1(\mathbb{R}^\infty) \to Gr_1(\mathbb{R}^\infty)$ is defined by $f(v_1) = \mathrm{span}(v_1)$. We use the following representation of $\mathrm{SO}(3)$:

$$\mathrm{SO}(3) = \{M \in \mathrm{M}_{3\times 3}(\mathbb{R}) \mid M^T M = I, \det M = 1\}.$$

Then D_2 is

$$\mathrm{D}_2 = \left\{ I, \begin{bmatrix} -1 & & \\ & -1 & \\ & & 1 \end{bmatrix}, \begin{bmatrix} -1 & & \\ & 1 & \\ & & -1 \end{bmatrix}, \begin{bmatrix} 1 & & \\ & -1 & \\ & & -1 \end{bmatrix} \right\} \subset SO(3).$$

For any $\begin{bmatrix} l \\ s \\ t \end{bmatrix} \in SO(3)$ with $l, s, t \in M_{1\times 3}$, the orbital of $\begin{bmatrix} l \\ s \\ t \end{bmatrix}$ is:

$$\begin{bmatrix} l \\ s \\ t \end{bmatrix}, \quad \begin{bmatrix} l \\ -s \\ -t \end{bmatrix}, \quad \begin{bmatrix} -l \\ s \\ -t \end{bmatrix}, \quad \begin{bmatrix} -l \\ -s \\ t \end{bmatrix}.$$

We claim that $\phi : \mathrm{SO}(3)/\mathrm{D}_2 \to Gr_1(\mathbb{R}^\infty) \times Gr_1(\mathbb{R}^\infty)$ is

$$\phi\left(\overline{\begin{bmatrix} l \\ s \\ t \end{bmatrix}}\right) = \left(\mathrm{span}\left(\begin{bmatrix} l & 0 & 0 & \cdots \end{bmatrix}\right), \mathrm{span}\left(\begin{bmatrix} s & 0 & 0 & \cdots \end{bmatrix}\right)\right).$$

Indeed, the pullback of ϕ and $f \times f$ is constructed as

$$S = X \times_{B\mathrm{D}_2} E\mathrm{D}_2$$
$$= \left\{ \left(\overline{\begin{bmatrix} l \\ s \\ t \end{bmatrix}}, (v_1, v_2) \right) \middle| \overline{\begin{bmatrix} l \\ s \\ t \end{bmatrix}} \in X,\ (v_1, v_2) \in V_1(\mathbb{R}^\infty) \times V_1(\mathbb{R}^\infty), \right.$$
$$\left. \mathrm{span}\left(\begin{bmatrix} l & 0 & 0 & \cdots \end{bmatrix}\right) = \mathrm{span}(v_1),\ \mathrm{span}\left(\begin{bmatrix} s & 0 & 0 & \cdots \end{bmatrix}\right) = \mathrm{span}(v_2) \right\}.$$

Since v_1, v_2 are orthonormal, we have $v_1 = [\pm l, 0, 0, \cdots]$, $v_2 = [\pm s, 0, 0, \cdots]$. Then by the follwoing correspondance, $S \simeq \mathrm{SO}(3)$:

$$\left(\overline{\begin{bmatrix} l \\ s \\ t \end{bmatrix}}, (l, s)\right) \mapsto \begin{bmatrix} l \\ s \\ t \end{bmatrix}, \left(\overline{\begin{bmatrix} l \\ s \\ t \end{bmatrix}}, (-l, s)\right) \mapsto \begin{bmatrix} -l \\ s \\ -t \end{bmatrix},$$

$$\left(\overline{\begin{bmatrix} l \\ s \\ t \end{bmatrix}}, (l, -s)\right) \mapsto \begin{bmatrix} l \\ -s \\ -t \end{bmatrix}, \left(\overline{\begin{bmatrix} l \\ s \\ t \end{bmatrix}}, (-l, -s)\right) \mapsto \begin{bmatrix} -l \\ -s \\ t \end{bmatrix}$$

3.2 Classifying II: A ball equipped with information like a bundle

In [26], it is established that $\pi_1\left(\mathrm{SO}(3)/\mathrm{D}_2\right) \simeq \mathrm{Q}$. In this section, we aim to provide a visualization of $\mathrm{SO}(3)/\mathrm{D}_2$ and $\pi_1\left(\mathrm{SO}(3)/\mathrm{D}_2\right)$ to offer an intuitive understanding of how eigenframes rotate.

Definition 3.2.1. The space of Hamiltonians is defined as:

$$\mathcal{H} = \{H = v_1^T v_1 + 2v_2^T v_2 + 3v_3^T v_3 | [v_1, v_2, v_3] \in \mathrm{SO}(3)/\mathrm{D}_2\}.$$

Remark 3.2.2. For any $[v_1, v_2, v_3] \in \mathrm{SO}(3)$, the following four configurations result in the same Hamiltonian H in $\mathcal{H}$, which explains why we quotient by

$$\mathrm{D}_2 : [v_1, v_2, v_3] \sim [-v_1, -v_2, v_3] \sim [-v_1, v_2, -v_3] \sim [v_1, -v_2, -v_3].$$

3.2.1 Visualizasion of $\mathrm{SO}(3)/\mathrm{D}_2$

Recall that $\mathrm{SO}(3) = \{M \in GL(3, \mathbb{R}) \mid M^T M = I, \det M = 1\}$, representing rotations that preserve orientation. Another way to describe $\mathrm{SO}(3)$ is by using rotation parameters- any rotation can be described by a pair $(\hat{r}, \theta)$, which means rotate along $\hat{r}$ by θ.

Definition 3.2.3. Let $\phi(\hat{r}, \theta)$ represent a rotation around the axis $\hat{r} \in S^2$ by an angle $\theta \in [0, 2\pi]$. Thus, we can describe $\mathrm{SO}(3)$ as:

$$\mathrm{SO}(3) = \{\phi(\hat{r}, \theta) | \hat{r} \in S^2, \theta \in [0, 2\pi]\}.$$

Next, we aim to reduce the parametrization of $\mathrm{SO}(3)$ and visualize it. Note that

$$\phi(\hat{r}, \theta) = \phi(-\hat{r}, 2\pi - \theta).$$

Specifically, $\phi(\hat{r}, \pi) = \phi(-\hat{r}, \pi)$. The first fact implies that we can always restrict the parameter θ to the interval $[0, \pi]$. For example,

$$\phi(\hat{x}, 3\pi/2) = \phi(\hat{x}, 2\pi - 3\pi/2) = \phi(\hat{x}, \pi/2).$$

This leads us to view $\mathrm{SO}(3)$ as a solid ball with radius π. Any point $\vec{t}$ in the ball represents the rotation $\phi(\vec{t}/|\vec{t}|, |\vec{t}|)$. For instance, the bold point in Figure 3-2 corresponds to $\phi(\hat{y}, \pi/2)$, representing a rotation by $\pi/2$ along the $\hat{y}$ axis. The second fact implies that one must identify antipodal points on the ball's boundary (Figure 3-3).

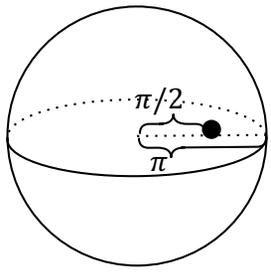

Figure 3-2 Solid ball representation of $\mathrm{SO}(3)$. The bold point is $\phi(\hat{y}, \pi/2)$, representing a rotation by $\pi/2$ along the $\hat{y}$ axis.

Therefore, $\mathrm{SO}(3)$ can be described as a ball of radius π with antipodal points on the

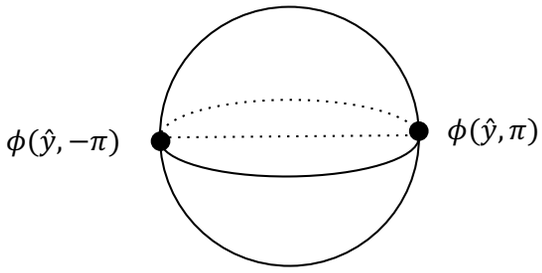

Figure 3-3 Antipodal points in the solid-ball representation of SO(3).

boundary identified. In other words,

$$\mathrm{SO}(3) \simeq B^3(\pi)/\sim,$$

where x equivalent to y if and only if $x, y \in \partial B^3(\pi)$ and $x = -y$.

Next, we turn our attention to visualizing $\mathrm{SO}(3)/\mathrm{D}_2$.

Fact 3.2.4. The dihedral group D_2 consists of the following elements:

$$\mathrm{D}_2 = \{\phi(\hat{x},\pi), \phi(\hat{y},\pi), \phi(\hat{z},\pi), id\}.$$

These elements can be represented by the four points shown in Figure 3-4.

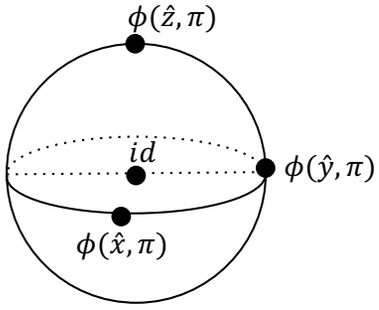

Figure 3-4 Points in the solid-ball representation of SO(3) corresponding to elements of D_2.

In summary, $\mathrm{SO}(3)/\mathrm{D}_2$ is a ball of radius π, with two operations applied: glue antipodal points and glue four points in Figure 3-4 to a point.

Fact 3.2.5. $\pi_1\big(\mathrm{SO}(3)/\mathrm{D}_2\big)$ is isomorphic to the quaternion group Q, i.e.,

$$\pi_1\big(\mathrm{SO}(3)/\mathrm{D}_2\big) \simeq \mathrm{Q} = \{\pm 1, \pm i, \pm j, \pm k\}.$$

Proposition 3.2.6. There is a bijection between the following spaces:

$\mathrm{SO}(3)/\mathrm{D}_2$ ↔ space of Hamiltonians ↔ space of eigenframes

Proof. The bijection is established as follows:

$$\mathrm{SO}(3)/\mathrm{D}_2 \leftrightarrow \{\text{space of Hamiltonians}\} \leftrightarrow \{\text{spaces of eigenframes}\}$$

$$\phi(\hat{r},\theta) \mapsto H = u_1^T u_1 + 2u_2^T u_2 + 3u_3^T u_3 \mapsto [u_1, u_2, u_3],$$

where $[e_1, e_2, e_3]$ is the standard frame in $\mathbb{R}^3$ and

$$[u_1, u_2, u_3] = \phi(\hat{r}, \theta)[e_1, e_2, e_3].$$

Hence, any loop in $\mathrm{SO}(3)/\mathrm{D}_2$ represents the evolution of an eigenframe. Consequently, any element in $\pi_1(\mathrm{SO}(3)/\mathrm{D}_2)$ can be interpreted as the evolution of an eigenframe.

Example 3.2.7. Consider loops L_1, L_5, and L_6 in Figure 3-5, where $\hat{x}$, $\hat{y}$, and $\hat{z}$ correspond to the first, second, and third eigenvectors, respectively.

Evolution of eigenframe on loop L_1: The first eigenvector ($\hat{x}$) remains fixed, while the second ($\hat{y}$) and third ($\hat{z}$) eigenvectors rotate by π.

Evolution of eigenframe on loop L_6: The second eigenvector ($\hat{y}$) stays fixed, with the first ($\hat{x}$) and third ($\hat{z}$) eigenvectors rotating by π.

Evolution of eigenframe on loop L_5: The third eigenvector ($\hat{z}$) is fixed, and the first ($\hat{x}$) and second ($\hat{y}$) eigenvectors rotate by π.

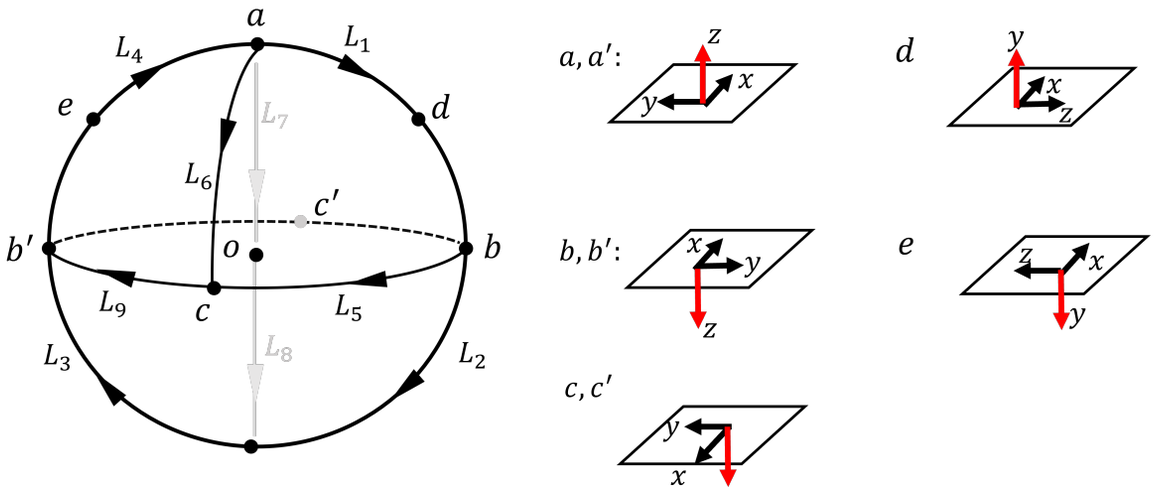

Figure 3-5 Loops in $\mathrm{SO}(3)/\mathrm{D}_2$ and the eigenframes at their endpoints.

Example 3.2.8. (Evolution on Loop L_1) Parametrization shown in Figure 3-6.

The rotation matrix for a rotation by angle ψ around the axis $[a_1, a_2, a_3]$ is given by:

$$\begin{bmatrix} \cos x + (1-\cos x)\,{a_1}^2 & (1-\cos x)\,a_1a_2 - \sin x a_3 & (1-\cos x)\,a_1a_3 + \sin x a_2 \\ (1-\cos x)\,a_1a_2 + \sin x a_3 & \cos x + (1-\cos x)\,{a_2}^2 & (1-\cos x)\,a_2a_3 - \sin x a_1 \\ (1-\cos x)\,a_1a_3 - \sin x a_2 & (1-\cos x)\,a_2a_3 + \sin x a_1 & \cos x + (1-\cos x)\,{a_3}^2 \end{bmatrix}.$$

In this case, $a_1 = 0$, $a_2 = \cos\theta$, $a_3 = \sin\theta$, and $\psi = \pi$. Therefore, the evolution of the eigenframe on loop L_1 involves the first eigenvector ($\hat{x}$) remaining fixed, while the second ($\hat{y}$) and third ($\hat{z}$) eigenvectors rotate by π.

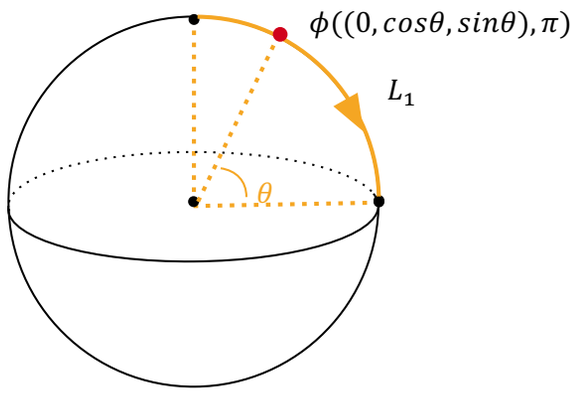

Figure 3-6 The loop L_1, parametrized by θ.

The eight points in Figure 3-7 represent a single point, and since loops must start and end at the same point, we only need to consider the loops shown in Figure 3-7.

In summary, all non-trivial loops can be represented by the loops (yellow lines) in Figure 3-7. (Arrows are omitted for simplicity.)

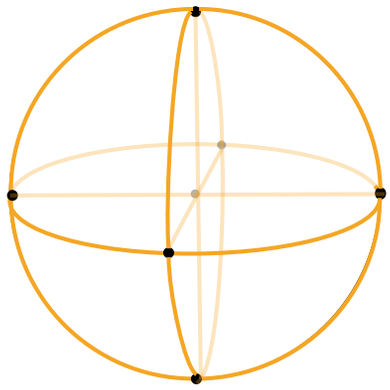

Figure 3-7 Primitive loops in $\mathrm{SO}(3)/\mathrm{D}_2$.

Next, we aim to explain $\pi_1\left(\mathrm{SO}(3)/\mathrm{D}_2\right)$.

Proposition 3.2.9. $L_1 = L_4$.

Proof. In L_1, $\hat{y}$ and $\hat{z}$ rotate clockwise, while in L_4^{-1}, $\hat{y}$ and $\hat{z}$ rotate counterclockwise. Hence, $L_1 = (L_4^{-1})^{-1} = L_4$.

Corollary 3.2.10. $L_1 = L_2 = L_3 = L_4$.

Proof. We have $L_3 = L_1$ and $L_2 = L_4$. With $L_1 = L_4$, we have $L_1 = L_2 = L_3 = L_4$.

Corollary 3.2.11. The order $|L_1| = 4$.

Proof. $L_1^4 = L_1L_2L_3L_4$ =trivial loop and obviously $L_1^2, L_1^3 \neq$ trivial loop.

Corollary 3.2.12. $L_1^2 = -1$.

Proof. $L_1^4 = 1$ so $L_1^2 = -1$.

Similarly, $L_7 = L_8$, and $|L_7| = 4$. Thus, we only need to focus on the $1/8$ ball. Since it's known that $\pi_1\left(\mathrm{SO}(3)/\mathrm{D}_2\right) \simeq \mathrm{Q}$, the visualization of $\pi_1\left(\mathrm{SO}(3)/\mathrm{D}_2\right)$ is shown in

Figure 3-8.

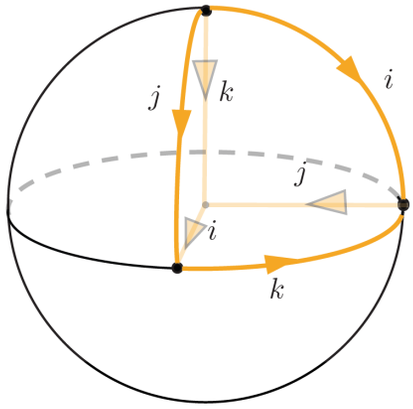

Figure 3-8 Loops in $SO(3)/D_2$ labeled by their corresponding group elements in Q.

Remark 3.2.13. Note that I have selected specific elements to illustrate properties. For instance, if we prove that $L_1 = L_2$, we also have $L_5 = L_9$ in Figure 3-5.

A conjecture is when two eigenvectors rotate by π, a degeneracy occurs between these two bands. Furthermore, orientations should be taken into account. For example, on L_1 (or L_2), the eigenvectors $\hat{y}$ and $\hat{z}$ rotate by π, so L_1 (or L_2), being a loop of charge i, encloses a degeneracy occurs between the 2^{nd} and 3^{rd} bands with positive orientation. In contrast, L_1^{-1} encloses a degeneracy that occurs between those bands with negative orientation.

Remark 3.2.14. For the loop -1, although the eigenframe evolution ends at its initial state, this is not a trivial loop. It is similar to a spin in physics, which must rotate by 4π to return to its initial state. A 2π rotation results in $-1 \neq 1$.

Compare our results with Relationship between Figure 3 A, B, C in [26]. This hypothesis implies that L_1L_2 surrounds two like-oriented degeneracies arising from the second and third bands. Therefore, L_1L_2 has a charge of -1. A similar analysis shows that L_7L_8 encloses two degeneracies with the same orientation formed by the first and second bands. The transformation in Figure 3A to C [26] represents the deformation from L_7L_8 to L_1L_2 on our ball, i.e., from $k^2 = -1$ to $i^2 = -1$ (see Figure 3-6(b)).

Quansheng Wu et al. proposed an experimental plan to verify the non-abelian charge experimentally [26]. The authors propose utilizing angle-resolved photoemission spectroscopy (ARPES) to observe the momentum-space nodal line (NL) configurations in elemental scandium (Sc) under various strain conditions. Scandium is identified as an ideal candidate because it possesses a hexagonal close-packed structure and exhibits weak spin-orbit coupling (SOC); the SOC-induced band splitting is less than 10 meV, which is

negligible relative to the resolution limit of contemporary ARPES instrumentation, thus validating the SOC-free approximation. The authors propose that the non-Abelian topological constraints can be verified by using ARPES to observe the strain-induced evolution of nodal line configurations in scandium, specifically the characteristic transfer and detachment of crossing points.

This visualization is valuable because the $\mathrm{SO}(3)/\mathrm{D}_2$ ball captures the rotational behaviors of frames within a loop, functioning similarly to a bundle. It presents a compelling image.

In the non-Hermitian case, if we could identify a group whose loop encompasses both the evolution of Hermitian and the evolution of eigenframes, we could apply the same approach. However, finding such a group appears to be quite challenging.

CHAPTER 4 REDUCTION

4.1 2-band real pseudo-Hermitian

In this section, we give a different way to recover results in [31], and this method can generalize to the discussion for 3-band real pseudo-Hermitian.

Definition 4.1.1. Let $\eta = diag[-1, 1]$. A 2-band real pseudo-Hermitian Hamiltonian is a 2×2 real matrix H satisfying $\eta H \eta = H^{\dagger}$.

Any 2-band real pseudo-Hermitian H has the form

$$H = \begin{bmatrix} a & b \\ -b & c \end{bmatrix}, \quad a, b, c \in \mathbb{R}.$$

The parametrized eigenpolynomial is $\lambda^2 - (a + c)\lambda + ac + b^2 = 0$. The eigenvalues are

$$\lambda_{\pm} = \frac{a + c \pm \sqrt{(a - c - 2b)\,(a - c + 2b)}}{2}.$$

For $b \neq 0$, the eigenvector $v_{\pm}$ to $\lambda_{\pm}$ is

$$v_{\pm} = \begin{bmatrix} \frac{c - \lambda_{\pm}}{b} \\ 1 \end{bmatrix} = \begin{bmatrix} \frac{c - a \mp \sqrt{(a-c-2b)(a-c+2b)}}{2b} \\ 1 \end{bmatrix}.$$

For $b = 0$, $\lambda_+ = max\{a, c\}$, $\lambda_- = min\{a, c\}$.

When $a > c$,

$$v_+ = \begin{bmatrix} s \\ 0 \end{bmatrix}, \quad v_- = \begin{bmatrix} 0 \\ t \end{bmatrix}, \quad s, t \text{ are real numbers.}$$

When $c > a$,

$$v_+ = \begin{bmatrix} 0 \\ s \end{bmatrix}, \quad v_- = \begin{bmatrix} t \\ 0 \end{bmatrix}, \quad s, t \text{ are real numbers.}$$

When $a = c$, eigenspace to the eigenvector has dimension 2.

From the computation, the degeneracy surfaces (surfaces that have only one eigenvalue) are $a - c - 2b = 0$, and $a - c + 2b = 0$. The two planes meet along the line l given by $y = 0$ and $z = x$.

We want to compute the configuration of the eigenvectors. Let's consider the eigenvector v_+ first. The main idea is to find points that have the same v_+.

We compute how parameter c affects eigenvectors. Let $c = s$ where $s \in \mathbb{R}$ is fixed. Then, we find that:

For b not equals to 0,

$$v_+(a+s,b,s) = \begin{bmatrix} \dfrac{s-(a+s) \mp \sqrt{(a+s-s-2b)(a+s-s+2b)}}{2b} \\ 1 \end{bmatrix}$$

$$= \begin{bmatrix} \dfrac{-a \mp \sqrt{(a-2b)(a+2b)}}{2b} \\ 1 \end{bmatrix} = v_+(a,b,0).$$

For b equals to 0 and $a + s > c$, this leads to a greater than 0. Hence,

$$v_+(a+s,0,s) = v_+(a,0,0).$$

For b equals to 0 and $c > a + s$, this leads to $a < 0$. Hence,

$$v_+(a+s,0,s) = v_+(a,0,0).$$

In summary, the equality

$$v_+(a+s,b,s) = v_+(a,b,0)$$

holds, that means, the configuration of v_+ has symmetry of translation $c = s$ plane along the singular line

$$l = \{(x,0,x) | x \in \mathbb{R}\}.$$

By symmetry of translation, we reduce the case to the $c = 0$ plane.

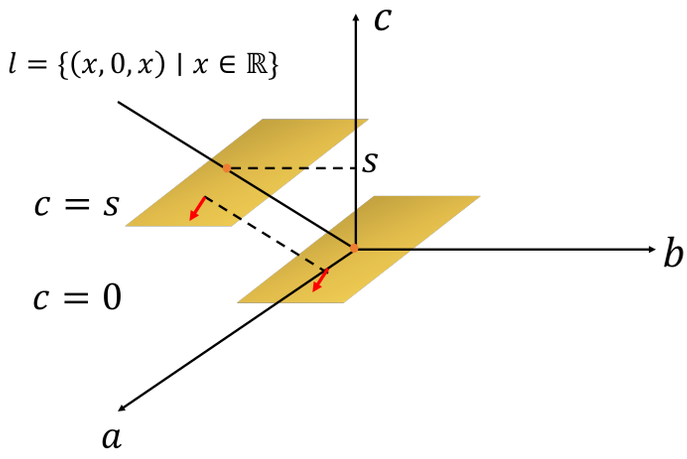

Figure 4-1 Translating the origin of the plane $c = 0$ along the line l produces a new plane with the same eigenvector distribution as the original one. The corresponding eigenvectors, depicted in red, remain unchanged under the translation.

We compute the configuration on the line $a = kb$ for a fixed $k \in \mathbb{R}$. By the above conclusion, we only consider c equals to 0.

When $b > 0$

$$v_+ = \begin{bmatrix} \frac{-a-\sqrt{a^2-4b^2}}{2b} \\ 1 \end{bmatrix} = \begin{bmatrix} -\frac{k}{2} - \sqrt{\frac{k^2}{4} - 1} \\ 1 \end{bmatrix}.$$

When $b < 0$

$$v_+ = \begin{bmatrix} \frac{-a-\sqrt{a^2-4b^2}}{2b} \\ 1 \end{bmatrix} = \begin{bmatrix} -\frac{k}{2} + \sqrt{\frac{k^2}{4} - 1} \\ 1 \end{bmatrix}.$$

When $b = 0, a > 0$

$$v_+ = \begin{bmatrix} x \\ 0 \end{bmatrix}, \quad x \in \mathbb{R}.$$

When $b = 0, 0 > a$

$$v_+ = \begin{bmatrix} 0 \\ x \end{bmatrix}, \quad x \in \mathbb{R}.$$

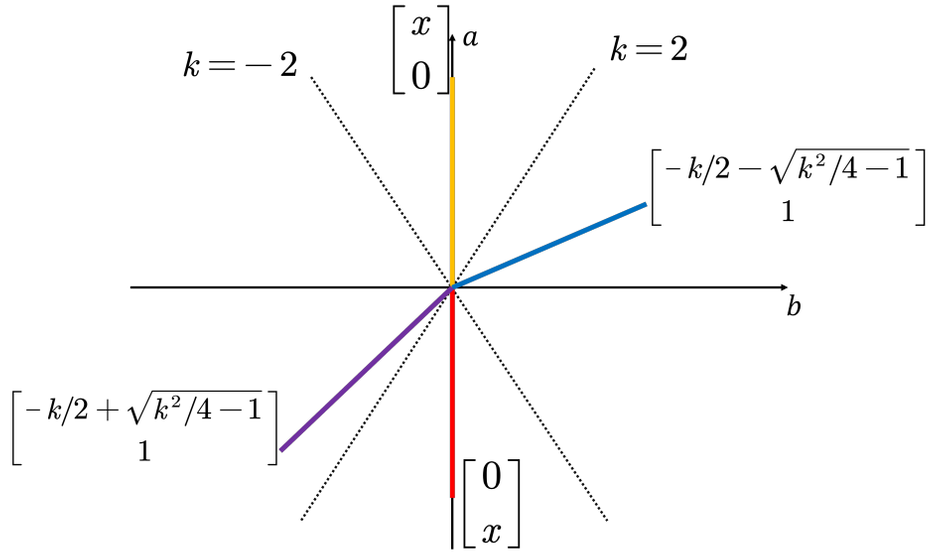

Figure 4-2 Parameter space (a, b) and the corresponding analytic expressions of the eigenvectors for different rays, where eigenvectors remain constant along each ray.

We compute limit at a-axis

When $b > 0$,

$$\lim_{k \to +\infty} -\frac{k}{2} - \sqrt{\frac{k^2}{4} - 1} = -\infty.$$

When $b > 0$,

$$\lim_{k\to-\infty} -\frac{k}{2} - \sqrt{\frac{k^2}{4} - 1} = 0^+.$$

When $b < 0$,

$$\lim_{k\to+\infty} -\frac{k}{2} + \sqrt{\frac{k^2}{4} - 1} = 0^-.$$

When $b < 0$,

$$\lim_{k\to-\infty} -\frac{k}{2} + \sqrt{\frac{k^2}{4} - 1} = +\infty.$$

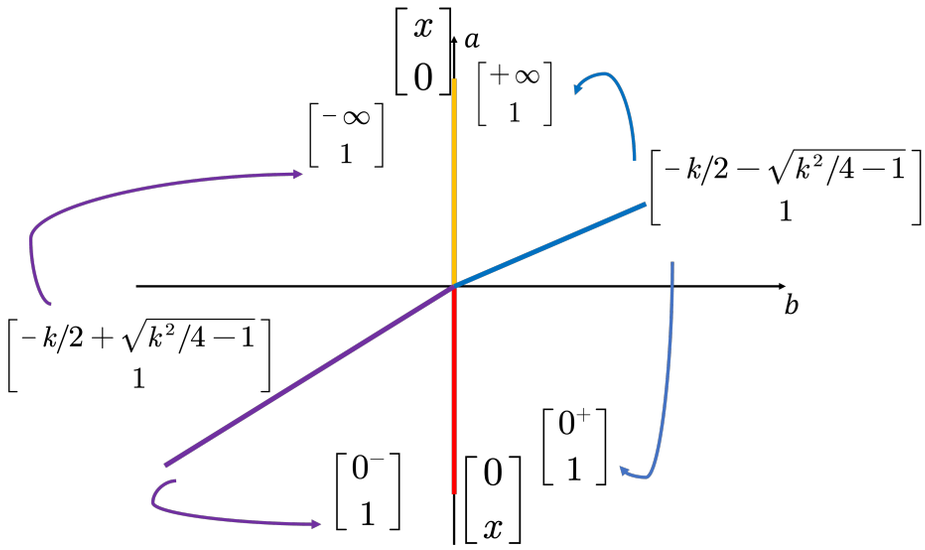

Figure 4-3 Limiting behavior of eigenvectors in the (a, b) parameter space as the rays approach the a-axis.

By computation of the limit at a-axis, we have conclusions: The eigenvector v_+ varies continuously on $\mathbb{R}^2 - \{(a, 0, 0)|a > 0\}$. Configuration near a-axis (first component is real) can be seen in Figure 4-3 and configuration in the region where the first component is complex can be seen in Figure 4-4.

In summary, the configuration of eigenvectors is S^1 identifies $A_1 \sim A_2$, $B_1 \sim B_2$ in Figure 4-5, which is the space $S^1 \vee S^1 \vee S^1$.

So $\pi_1(S^1 \vee S^1 \vee S^1) = \mathbb{Z} * \mathbb{Z} * \mathbb{Z}$ classifies the singularity, coinciding with the result in [31].

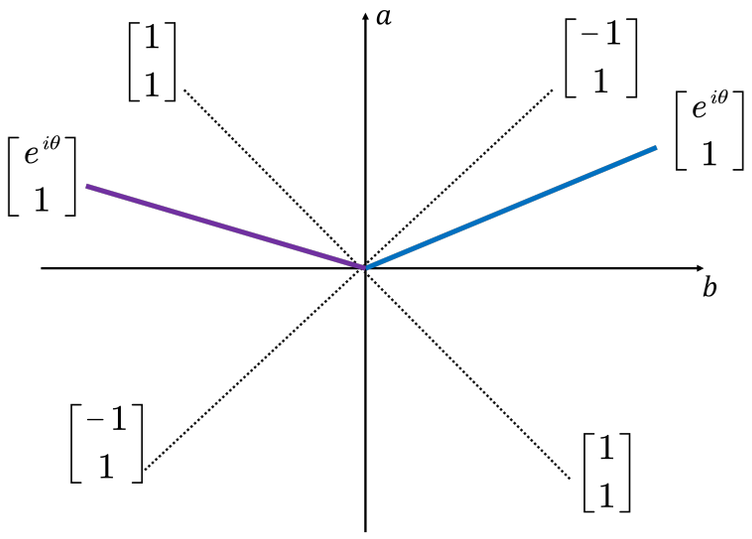

Figure 4-4 Eigenvectors in the complex regime, which remain constant along each ray.

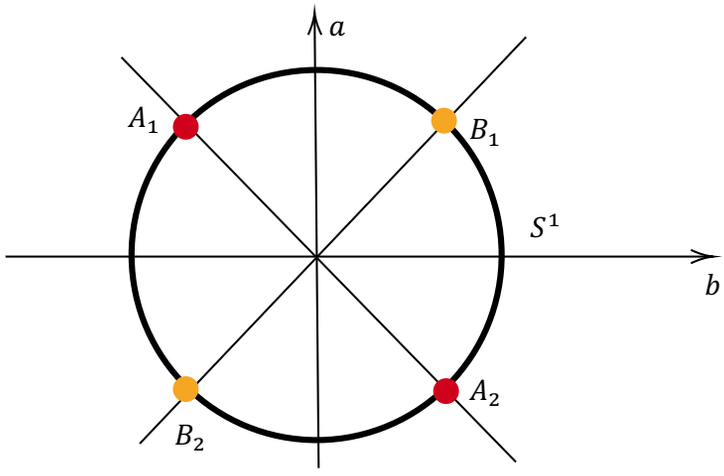

Figure 4-5 Points A_1 and A_2 on S^1 correspond to the same eigenvector, and similarly for B_1 and B_2.

4.2 Reducing number of parameters in 3-band real pseudo-Hermitian

In this section, we reduce the parameter space $\mathbb{R}^6$ of a 3-band real pseudo-Hermitian matrix to $\mathbb{R}^4$ by symmetry of eigenpolynomials.

Definition 4.2.1. Let $\eta = diag[-1, 1, 1]$. The 3-band real pseudo Hermitian H is a 3×3 matrix H satisfying $\eta H \eta = H^{\dagger}$.

The 3-band real pseudo Hermitian H is of the form

$$\begin{bmatrix} a & b & c \\ -b & d & e \\ -c & e & f \end{bmatrix}, \quad a, b, c, d, e, f \in \mathbb{R}.$$

We show the eigenvectors have translation symmetry. The characteristic polynomial of H is

$$(a-\lambda)(d-\lambda)(f-\lambda) + b^2(f-\lambda) + c^2(d-\lambda) - e^2(a-\lambda) - 2bce = 0 \qquad (1)$$

The eigenvector is the solution to

$$\begin{bmatrix} a-\lambda & b & c \\ -b & d-\lambda & e \\ -c & e & f-\lambda \end{bmatrix} \begin{bmatrix} x_1 \\ x_2 \\ x_3 \end{bmatrix} = \begin{bmatrix} 0 \\ 0 \\ 0 \end{bmatrix}.$$

Consider the transformation (a, b, c, d, e, f) shift a, d, f by s and let $a' = a + s$, $d' = d + s$, $f' = f + s$. Then the eigenfunction becomes

$$\begin{aligned} &(a+s-\lambda')(d+s-\lambda')(f+s-\lambda') + b^2(f+s-\lambda') + c^2(d+s-\lambda') \\ &\quad - e^2(a+s-\lambda') - 2bce \\ &= (a-(\lambda'-s))(d-(\lambda'-s))(f-(\lambda'-s)) + b^2(f-(\lambda'-s)) + c^2(d-(\lambda'-s)) \\ &\quad - e^2(a-(\lambda'-s)) - 2bce \\ &= 0 \end{aligned} \qquad (2)$$

Comparison with (1) and (2), we have $\lambda' - s = \lambda$. Therefore, the equation

$$\begin{bmatrix} a+s-\lambda' & b & c \\ -b & d+s-\lambda' & e \\ -c & e & f+s-\lambda' \end{bmatrix} \begin{bmatrix} x_1 \\ x_2 \\ x_3 \end{bmatrix} = \begin{bmatrix} 0 \\ 0 \\ 0 \end{bmatrix}$$

is equal to the equation

$$\begin{bmatrix} a-\lambda & b & c \\ -b & d-\lambda & e \\ -c & e & f-\lambda \end{bmatrix}\begin{bmatrix} x_1 \\ x_2 \\ x_3 \end{bmatrix}=\begin{bmatrix} 0 \\ 0 \\ 0 \end{bmatrix}.$$

That means, translation preserves eigenspace.

We show that the eigenvectors have strech symmetry. Consider the transformation: each coordinate of (a,b,c,d,e,f) is multiplied by k when $k \neq 0$.

The eigen function becomes

$$(ka-\lambda')(kd-\lambda')(kf-\lambda')+k^2b^2(kf-\lambda')+k^2c^2(kd-\lambda')-k^2e^2(ka-\lambda')-2k^3bce=0$$

Devide it by k^3, we obtain

$$(a-\lambda'/k)(d-\lambda'/k)(f-\lambda'/k)+b^2(f-\lambda'/k)+c^2(d-\lambda'/k)-e^2(a-\lambda'/k)-2bce=0$$

Comparison with (1), we have $\lambda'/k=\lambda$. Therefore,

$$\begin{bmatrix} ka-\lambda' & kb & kc \\ -kb & kd-\lambda' & ke \\ -kc & ke & kf-\lambda' \end{bmatrix}\begin{bmatrix} x_1 \\ x_2 \\ x_3 \end{bmatrix}=\begin{bmatrix} 0 \\ 0 \\ 0 \end{bmatrix}$$

has the same solution as

$$\begin{bmatrix} a-\lambda & b & c \\ -b & d-\lambda & e \\ -c & e & f-\lambda \end{bmatrix}\begin{bmatrix} x_1 \\ x_2 \\ x_3 \end{bmatrix}=\begin{bmatrix} 0 \\ 0 \\ 0 \end{bmatrix}$$

by primary row transformation.

Hence, the stretch transformation preserves the eigenspace, i.e., we have:

$$v_i(a+s,b,c,d+s,e,f+s)=v_i(a,b,c,d,e,f), \quad i=1,2,3,$$

and

$$v_i(ka,kb,kc,kd,ke,kf)=v_i(a,b,c,d,e,f), \quad k\neq 0, \quad i=1,2,3.$$

By above discussion, we can always set one of a,d,f to 0 and one of the other elements to 1. This reduces parameters from $\mathbb{R}^6$ to $\mathbb{R}^4$, which is helpful for further work.

CHAPTER 5 INTERSECTION HOMOLOGY OF THE BASE SPACE

5.1 Intersection homology

In recent years, intersection homology has become an indispensable tool for studying the topology of singular spaces. While the main results of usual homology theories often fail for singular spaces, intersection homology effectively recovers these properties, bridging this critical gap. Appropriate reference for intersection homology/homotopy are [35–41].

Definition 5.1.1. A filtration is a sequence of closed subsets of X:

$$X_n \supseteq X_{n-1} \supseteq \cdots \supseteq X_2 \supseteq X_1 \supseteq X_0 \supseteq X_{-1}$$

The connected component of $X_i - X_{i-1}$ is called a stratum.

In application, X_i is always i-dimensional singularities of X A stratum in $X_i - X_{i-1}$ can be viewed as i-dimensional spaces without lower dimensional singularities.

Let X be a filtered simplicial complex. We say i-simplex σ is in general position with respect to a stratum S if $\dim(\sigma \cap S) \leqslant \dim(\sigma) + \dim(S) - n$ for every stratum S of X. It is always possible for us to move an i-simplex to be in a general position with stratum S in manifolds. However, this is not true in singular spaces.

Definition 5.1.2. Let X be a filtered space of formal dimension n. Let $\mathcal{F}$ denote the set of strata of X. A perversity on X is a function $\bar{p} : \mathcal{F} \to \mathbb{Z}$ such that $\bar{p}(S) = 0$ if $S \subset X_n - X_{n-1}$.

Definition 5.1.3. i-simplex σ is called $\bar{p}$-allowable if

$$\dim(\sigma \cap S) \leqslant \dim(\sigma) + \dim(S) - n + \bar{p}(S)$$

for every stratum S of X.

This condition controls how far a simplex is allowed to deviate from general position. If it is too strange, we do not acknowledge it as an allowed i-chain, but if it is not too strange, we accept it as an allowable i-simplex.

Definition 5.1.4. Let X be a filtered simplicial complex with filtration

$$X_n \supset X_{n-2} \supseteq \cdots \supseteq X_0.$$

An i-chain ζ is called $\bar{p}$-allowable if every simplex in ζ and $\partial\zeta$ is $\bar{p}$-allowable. Define the

group $I^{\bar{p}}C_i(X)$ be the subset of $C_i(X)$ consisting of $\bar{p}$-allowable i-chains.

It can be shown that the chain complex $(C_*(X), \partial)$ restricts to a chain complex $(I^{\bar{p}}C_*(X), \partial)$.

Definition 5.1.5. The intersection homology groups are given by $I^{\bar{p}}H_i(X) = H_i(I^{\bar{p}}C_\cdot(X))$

For a topological space, we require that PL intersection homology is independent of triangulation. Let's define PL homology first.

Definition 5.1.6. By a triangulation of a topological space X, we mean a pair $T = (K, h)$ such that: K is a simplicial complex that is locally finite and $h : |K| \to X$ is a homeomorphism.

Remark 5.1.7. Local finiteness means: every point $x \in |K|$ admits a neighborhood U that intersects only finitely many simplices.

Definition 5.1.8. Two triangulations $T = (K, h)$ and $S = (L, j)$ are said to be equivalent precisely when $j^{-1}h$ is a simplicial isomorphism.

Definition 5.1.9. A subdivision of a triangulation $T = (K, h)$ is a triangulation $T' = (K', h)$, where K' is a subdivision of K.

Remark 5.1.10. Two triangulations $T = (K, h)$ and $S = (L, j)$ are said to admit a common refinement if one can find a subdivision $T' = (K', k)$ of T and a subdivision $S' = (L', \ell)$ of S for which the induced map $f : K' \to L'$ is a simplicial isomorphism.

Fact 5.1.11. $(\mathcal{T}, \leqslant)$ is a directed set (i.e., the relationship $\leqslant$ satisfying (1) transitive, (2) reflexive, (3) for any $T, S \in \mathcal{T}$, $\exists W \in \mathcal{T}$ such that $T \leqslant W$ and $S \leqslant W$).

Definition 5.1.12. Let $(X, \mathcal{T})$ be a PL space. For $T = (K, k) \in \mathcal{T}$, define $C_*^T(X) = C_*(|K|)$.

Definition 5.1.13. Let

$$T = (K, k) \leqslant T' = (K', k')$$

in $\mathcal{T}$. We define a map

$$C_*^T(X) = C_*(|K|) \longrightarrow C_*(|K'|) = C_*^{T'}(X), \qquad \sigma \mapsto \sum_{\tau_\sigma \subseteq |\sigma|} \tau_\sigma.$$

For $\xi = \sum_i a_i \sigma_i$, the map is

$$\xi \mapsto \sum_i a_i \sum_{\tau_{\sigma_i} \subseteq |\sigma_i|} \tau_{\sigma_i}$$

$$\sigma \mapsto \sigma_1 + \sigma_2$$

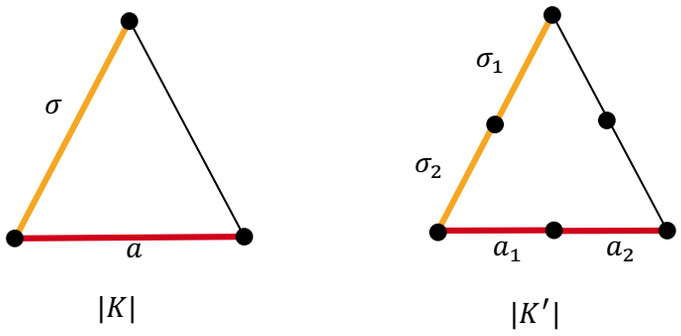

Figure 5-1 An example for subdivision chain map.

$$\sigma + 2a \mapsto \sigma_1 + \sigma_2 + 2(a_1 + a_2).$$

It is straightforward to verify that with the above data, we can define a direct limit as follows:

Definition 5.1.14. $C_*^{\mathcal{T}}(X) := \varinjlim_{T\in\mathcal{T}} C_*^T(X)$, where $C_*^T(X) = C_*(|K|)$ for $T = (K,k)$.

Actually, we do not need all triangulations in $\mathcal{T}$. We only need a subset of $\mathcal{T}$ containing all subdivisions of a fixed triangulation T_0.

Proposition 5.1.15. Let X be a PL space with admissible triangulation $\mathcal{T}$. Let

$$T_0 = (K,k) \in \mathcal{T}$$

and let $\mathcal{T}_0$ be the subset of $\mathcal{T}$ consisting of subdivision of T_0. Then

$$C_*^{\mathcal{T}}(X) = \varinjlim_{T\in\mathcal{T}} C_*^T(X) \cong \varinjlim_{T\in\mathcal{T}_0} C_*^T(X).$$

Definition 5.1.16. X is a PL space. Define PL homology of PL space $(X,\mathcal{T})$ as

$$\mathcal{H}_*(X) := H_*(C_\bullet^{\mathcal{T}}(X)).$$

Proposition 5.1.17. Let X be a PL space. Then $\mathcal{H}_*(X) \cong H_*(X)$, where $H_*(X)$ can be singular or simplicial homology with respect to any triangulation.

Remark 5.1.18. PL intersection homology (defined later) may not be isomorphic to $H_*(X)$ in general.

Definition 5.1.19. Let X be a PL filtered space for which each skeleton X_i is a subcomplex in every admissible triangulation.

Define $I^{\bar{p}}C_*^{\mathcal{T}}(X) := \varinjlim_{T\in\mathcal{T}} I^{\bar{p}}C_*^T(X)$, where $I^{\bar{p}}C_*^T(X) := I^{\bar{p}}C_*(|K|)$.

Remark 5.1.20. Filtration and perversity of X can "move to" $|K|$ by homeomorphism k.

Definition 5.1.21. We define the PL intersection homology of PL space $(X,\mathcal{T})$ as

$$I^{\bar{p}}\mathcal{H}_*(X) := H_*(I^{\bar{p}}C_\bullet^{\mathcal{T}}(X)) \cong \varinjlim_{T\in\mathcal{T}_0} H_*(I^{\bar{p}}C_\bullet^T(X)) = \varinjlim_{T\in\mathcal{T}_0} I^{\bar{p}}H_*^T(X),$$

where

$$I^{\bar{p}}H_*^T(X) = I^{\bar{p}}H_*(|K|)$$

for $T = (K, k)$.

Definition 5.1.22. Let L be a subcomplex of K. Then L is termed a full subcomplex if whenever a simplex $\sigma \in K$ has all its vertices lying in L, it follows that $\sigma \in L$.

Definition 5.1.23. An admissible triangulation T of a PL filtered space X with filtration $\{X_i\}$ is called a full triangulation if all X_i are full subcomplexes of X.

Theorem 5.1.24. Let X be a PL filtered space. Let T be a full triangulation and T' be an arbitrary subdivision of T. Then

$$I^{\bar{p}}C_*^T(X) \longrightarrow I^{\bar{p}}C_*^{T'}(X)$$

is an isomorphism.

Corollary 5.1.25. We have

$$\mathcal{H}_*(X) = \varinjlim_{T' \in \mathcal{T}_0} H_*\left(I^{\bar{p}}C_\bullet^{T'}(X)\right) = H_*\left(\varinjlim_{T' \in \mathcal{T}_0} I^{\bar{p}}C_\bullet^{T}(X)\right) = H_*\left(I^{\bar{p}}C_\bullet^{T}(X)\right) = I^{\bar{p}}H_*^T(X).$$

5.2 Computation of $\mathbb{R}^2$ with two degeneracy lines

In this section, we compute the example in Figure 5-2. It is $\mathbb{R}^2$ with two degeneracy lines L_1 and L_2.

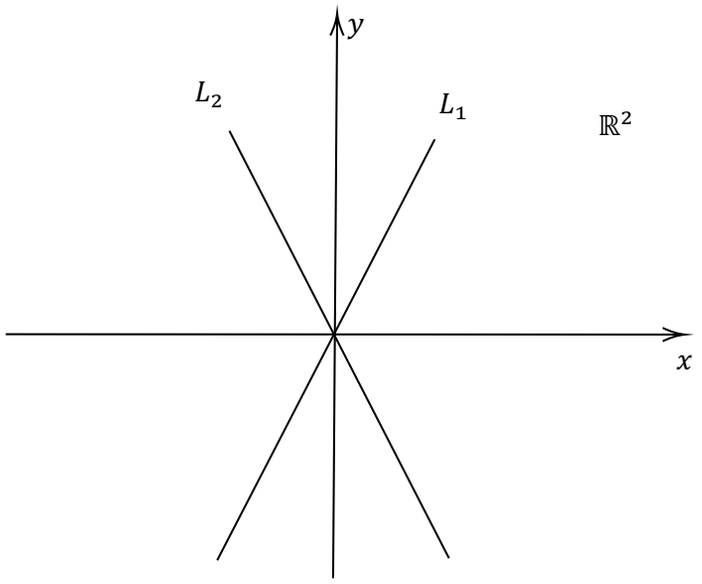

Figure 5-2 $\mathbb{R}^2$ with two degeneracy lines L_1 and L_2.

We have filtration $X_2 \supseteq X_1 \supseteq X_0 \supseteq X_{-1}$, where $X_2 = \mathbb{R}^2$, $X_1 = L_1 \cup L_2$, $X_0 = L_1 \cap L_2$.

The strata are shown in Figure 5-3. We only need to choose a full triangulation to compute PL intersection homology. We choose a triangulation in Figure 5-4. The computation proceeds by classifying i-simplices into several types (see Figure 5-5).

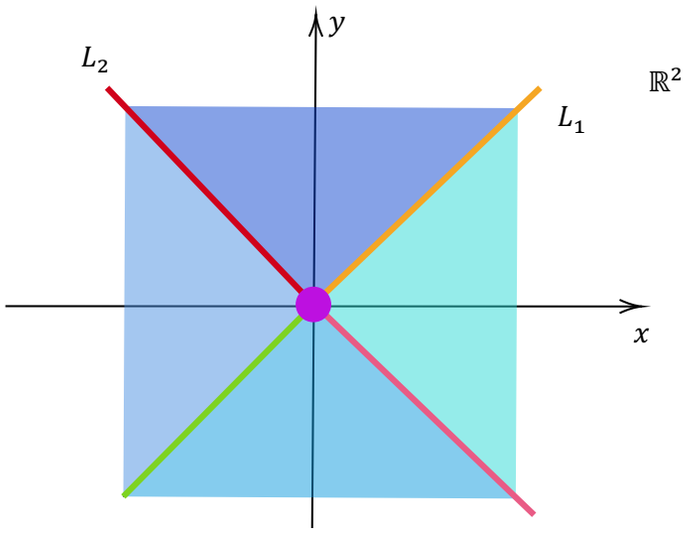

Figure 5-3 Strata of X. There are four strata in $X_2 - X_1$, depicted in blue; There are four strata in $X_1 - X_0$, depicted in red, pink, yellow and green; There is one stratum in X_0, depicted in purple.

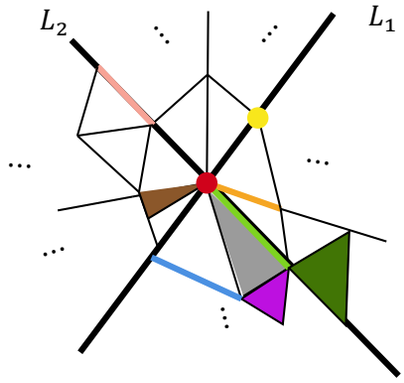

Figure 5-4 A full triangulation of X.

We assume perversity are same on O_1, O_2, O_3, O_4:

$$\bar{p} : \{\text{Strata of X}\} \to \mathbb{Z}$$

$$R_i \mapsto 0, O_i \mapsto \bar{p}(1), i \text{ from 1 to 4, and } T \mapsto \bar{p}(2)$$

The following steps compute the allowability condition for simplices of dimension 0, 1, 2. Let η be any 2-simplex. It is allowable if

$$\dim(\eta \cap X_0) \leqslant 2 - 2 + \bar{p}(2) \text{ and } \dim(\eta \cap (X_1 - X_0)) \leqslant 2 - 1 + \bar{p}(1).$$

0-simplex:
type I_0: Intersects with X_0
type II_0: Intersects with $X_1 - X_0$

1-simplex:
type I_1: Only intersects with $X_1 - X_0$ of dim 1
type II_1: Only intersects with $X_1 - X_0$ of dim 0
type III_1: Intersects with $X_1 - X_0, X_0$
type IV_1: Only intersects with X_0

2-simplex:
type I_2: Intersects with $X_1 - X_0, X_0$
type II_2: Only intersects with $X_1 - X_0$ of dim 1
type III_2: Only intersects with $X_1 - X_0$ of dim 0
type IV_2: Only intersects with X_0

Figure 5-5 Types of simplices: we ignore the intersection with $X_2 - X_1$ since we can always ignore the allowability condition on regular strata. The sub-index of a type denotes the dimension of the simplex, and the corresponding examples are depicted in the same color in Figure 5-4.

Let e be any 1-simplex. It is allowable if

$$\dim(e \cap X_0) \leqslant 1 - 2 + \bar{p}(2) \text{ and } \dim(e \cap (X_1 - X_0)) \leqslant 1 - 1 + \bar{p}(1).$$

Let v be any 0-simplex. It is allowable if

$$\dim(v \cap X_0) \leqslant -2 + \bar{p}(2) \text{ and } \dim(v \cap (X_1 - X_0) \leqslant -1 + \bar{p}(1)).$$

These allowability conditions suggest that we need to discuss the problem in 16 cases based on the value ranges of $\bar{p}(1)$ and $\bar{p}(2)$. In each of the 16 cases, we have labeled the allowable simplices for that case; see Figure 5-6.

Remark 5.2.1. Figure 5-6 is obtained by combining three figures in Figure 5-7.

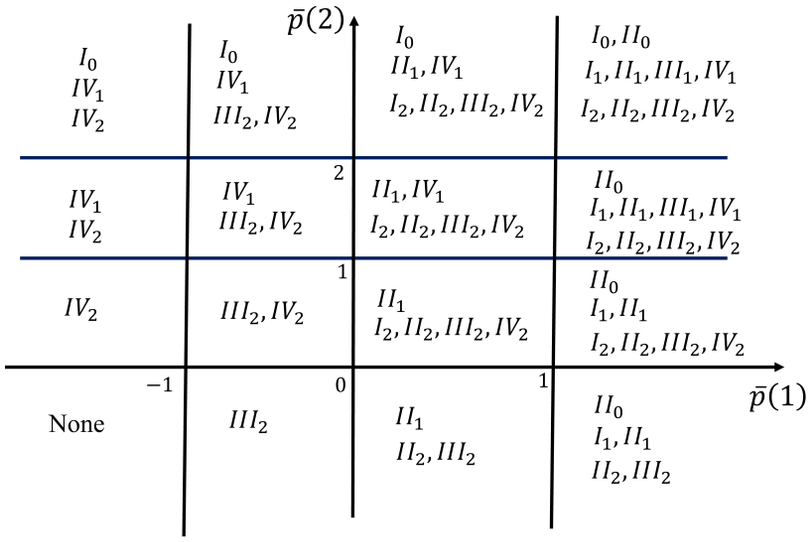

Figure 5-6 The allowable simplex type in each case. Note that all cases contain points on the line. e.g., the bottom right box is $\bar{p}(2) < 0, \bar{p}(1) \geqslant 1$.

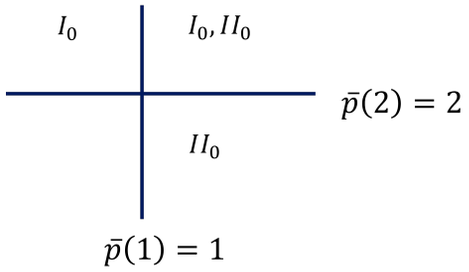

(a) Allowable 0-simplices for different perversities.

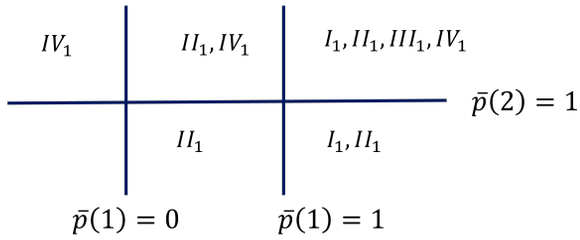

(b) Allowable 1-simplices for different perversities.

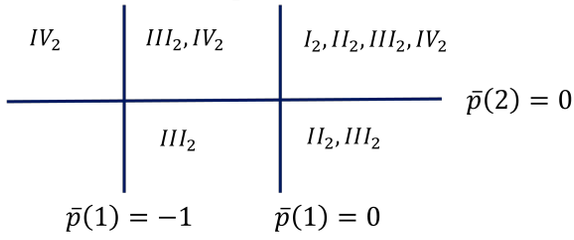

(c) Allowable 2-simplices for different perversities.

Figure 5-7 Allowability conditions for simplices of different dimensions.

Example 5.2.2. Consider the case $1 \geqslant \bar{p}(2) < 2, \bar{p}(1) < -1$. In this case, we can see in Figure 5-6 that types IV_1 and IV_2 are allowable. With IV_1, any allowable 0-simplex can be homologous to each other, so $I^{\bar{p}}H_0 = \mathbb{Z}$. The allowable 1-cycles lie in regular strata, so all 1-cycles are trivial, thus $I^{\bar{p}}H_1 = 0$. There is no 2-cycle, so $I^{\bar{p}}H_2 = 0$.

The other cases are obtained similarly. The computation results are shown in Fig-

ure 5-8.

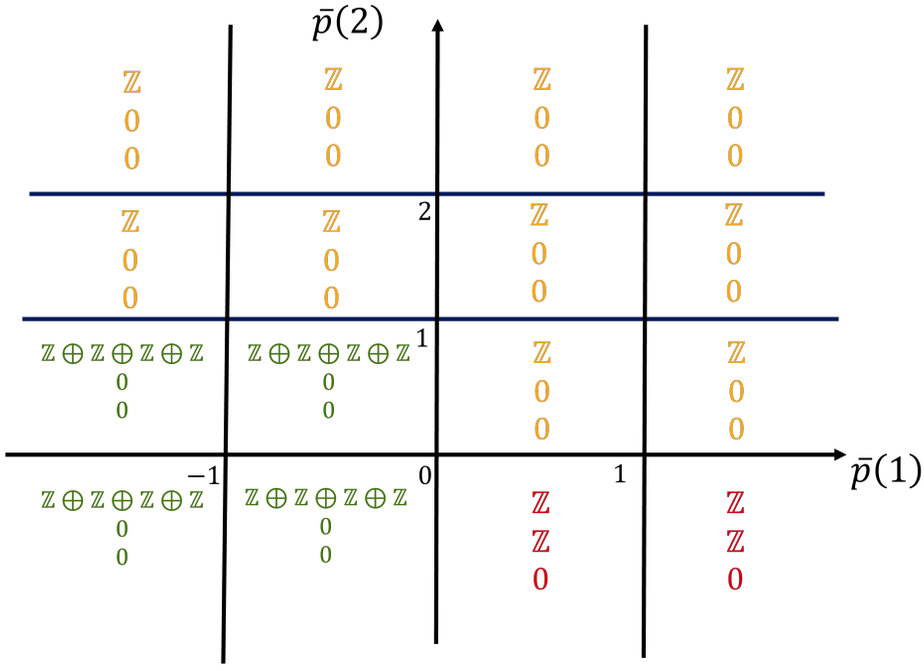

Figure 5-8 Intersection homology of $\mathbb{R}^2$ with two singular lines. From top to bottom is $I^{\bar{p}}H_0$, $I^{\bar{p}}H_1$, $I^{\bar{p}}H_2$.

Example 5.2.3. We provide some example loops in Figure 5-9. For $\bar{p}(1) < 0, \bar{p}(2) \geqslant 1$, loops in Figure 5-9 (a) are trivial, i.e., they are bounded by allowable 2-chains. For $\bar{p}(1) < 0, \bar{p}(2) < 1$, the only allowable loops in (b) are trivial loops in regular stratum. Consider the case $\bar{p}(1) \geqslant 1, \bar{p}(2) \leqslant 0$ in (c), the loop 1, 2, 3 are trivial and loop 4 is nontrivial, generated $I^{\bar{p}}H_1 = \mathbb{Z}$.

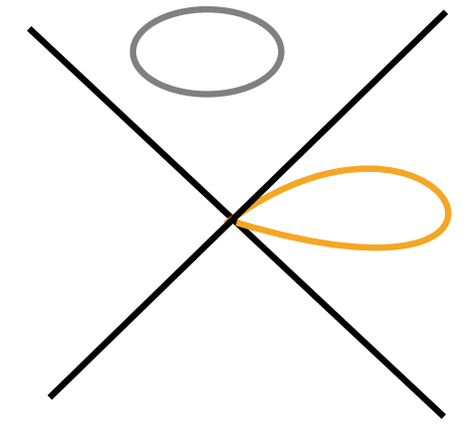

(a)

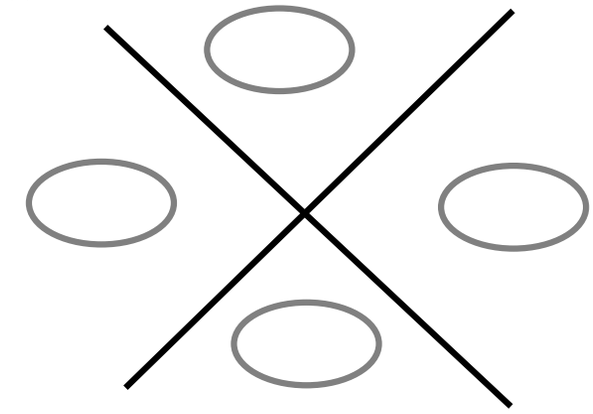

(b)

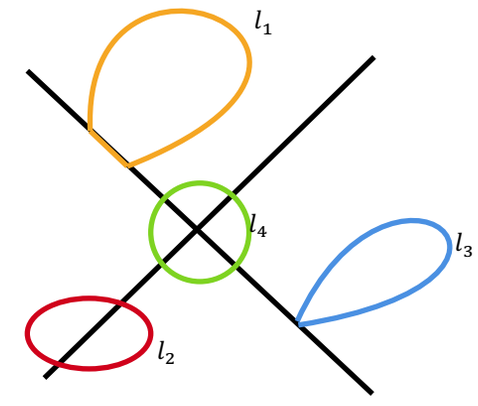

(c)

Figure 5-9 Examples of loops.

In Figure 5-8, from yellow region to green region, we "see" the two singular lines; From yellow region to red region, we "see" the singular point at the origin. It's equal to regular homology $H_*(\mathbb{R}^2)$ for nonnegative perversity. More discussion can be seen in Conjecture 3.4. We divide the results in Figure 5-8 into four parts: A, B, C, D, see Figure 5-10. In part A, type IV_1 are allowable so $I^{\bar{p}}H_0 = \mathbb{Z}$. The only allowable 1-simplex is IV_1,

so any 1-cycle lies in regular strata or touches X_0. Hence $I^{\bar{p}}H_1 = 0$. In part B, all 2-simplex are allowable, so $I^{\bar{p}}H_1 = 0$. Since type II_1 is allowable in any case, $I^{\bar{p}}H_0 = \mathbb{Z}$. In part C, four types of 1-simplices are not allowable, so there are four path components, and thus $I^{\bar{p}}H_0 = \mathbb{Z} \oplus \mathbb{Z} \oplus \mathbb{Z} \oplus \mathbb{Z}$. All allowable 1-cycle lie in the regular stratum, so $I^{\bar{p}}H_1 = 0$. In part D, the type II_1 is allowed, so $I^{\bar{p}}H_0 = \mathbb{Z}$. There is a nontrivial 1-cycle that encloses the origin.

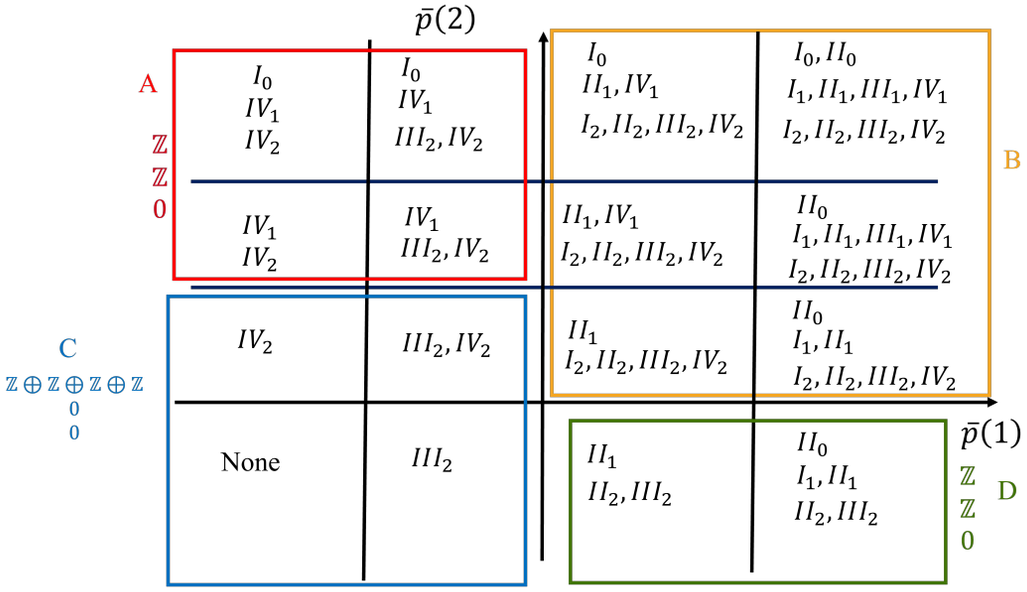

Figure 5-10 Division of the results into four parts: A, B, C, and D.

Conjecture 5.2.4. With nonnegative perversity, the intersection homology of a smooth 2-manifold is the same as the general homology.

Sketch of the proof. Let η be any 2-simplex. It's allowable if

$$\dim(\eta \cap X_0) \leqslant 2 - 2 + \bar{p}(2) \text{ and } \dim(\eta \cap (X_1 - X_0)) \leqslant 2 - 1 + \bar{p}(1).$$

When perversity is nonnegative, all 2-simplices are allowable up to homology, i.e., $C_2^{\bar{p}}(X) = C_2(X)$ up to homology.

Let e be any 1-simplex. It is allowable if

$$\dim(e \cap X_0) \leqslant 1-2+\bar{p}(2) = \bar{p}(2)-1 \text{ and } \dim(e \cap (X_1 - X_0)) \leqslant 1-1+\bar{p}(1) = \bar{p}(1).$$

From the condition, we find that all 1-simples intersect with $X_1 - X_0$ of 0-dimension, and not containing X_0 is allowable. Since all 2-simplices are allowable and it is a smooth manifold, we can always (need to be proved) homologously add a 1-simplex to intersect with $X_1 - X_0$ of 0-dimension and do not contain X_0. Hence all 1-simplex is allowable up to homology, i.e., $C_1^{\bar{p}}(X) = C_1(X)$ up to homology.

Let v be any 0-simplex. It is allowable if

$$\dim(v \cap X_0) \leqslant -2 + \bar{p}(2) \text{ and } \dim(v \cap (X_1 - X_0) \leqslant -1 + \bar{p}(1)).$$

We find that all 0-simplex not intersecting X_1 are allowable from the condition. Since all 1-simplices are allowable and we are in a smooth manifold, we can always homologize a 0-simplex to a 0-simplex not intersecting X_1. So, all 0-simplex is allowable up to homology, $C_0^{\bar{p}}(X) = C_0(X)$ up to homology.

Hence, $I^{\bar{p}}H_*(X) = H_*(X)$.

5.3 Compute $\mathbb{R}^2$ with one singular point

The parametrization space of a 2-band Hermitian system is $\mathbb{R}^2$ with a single singularity at the origin, see Figure 5-11. The types of simplices are in Figure 5-12, and the allowable simplices in each case are in Figure 5-13. By a similar calculation, the results are in Figure 5-30.

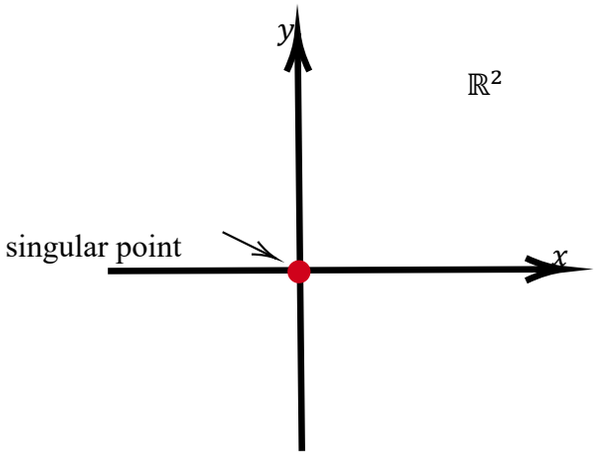

Figure 5-11 $\mathbb{R}^2$ with a singular point.

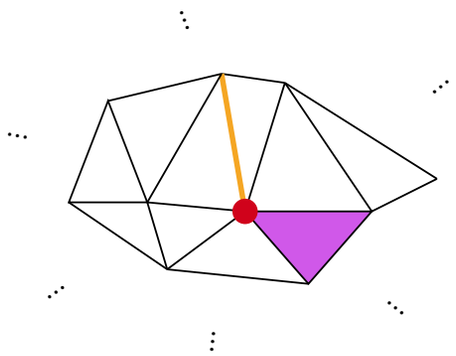

0-simplex: type I_0 Intersects with X_0

1-simplex: type I_1 Intersects with X_0

2-simplex: type I_2 Intersects with X_0

Figure 5-12 Types of simplices.

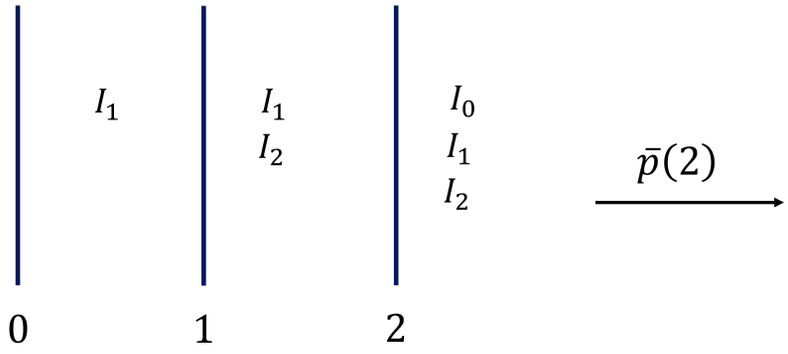

Figure 5-13 Allowable simplices in each case.

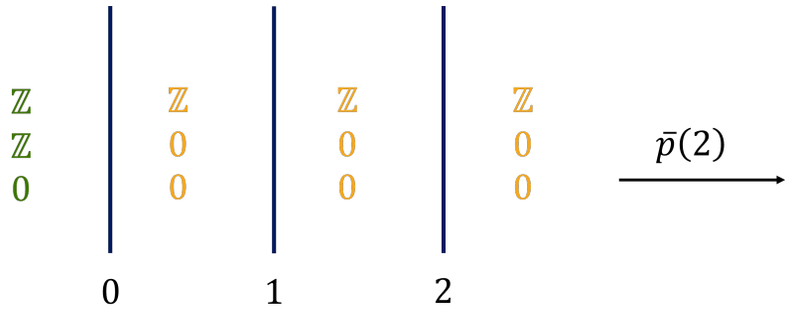

Figure 5-14 Intersection homology of $\mathbb{R}^2$ with one singular point. From top to bottom is $I^{\bar{p}}H_0$, $I^{\bar{p}}H_1$, $I^{\bar{p}}H_2$.

From the yellow region to the green region, the $I^{\bar{p}}H_1(\mathbb{R}^2)$ varies from 0 to $\mathbb{Z}$, meaning that we detect the singular point at the origin.

5.4 Intersection homology of swallowtail

We consider the filtered space $\mathbb{R}^3$ with filtration $X_3 \supset X_2 \supset X_1 \supset X_0 \supset X_{-1} = \emptyset$ where $X_3 = \mathbb{R}^3$, X_2 is the yellow surface, X_1 is the red and purple intersection lines and X_0 is the origin point, see Figure 5-15. Since there is no nontrivial 3-cycle in $C_3(\mathbb{R}^3)$, so is $I^{\bar{p}}C_3(\mathbb{R}^3)$. Thus $I^{\bar{p}}H_3(\mathbb{R}^3) = 0$.

Type of 0-simplex and 1-simplex is shown in Figure 5-16. The allowable 1 and 0-simplex for different perversity is shown in Figure 5-17.

Method to obtain Figure 5-17: Here we take type III_1 for example. The allowable 1-simplex e satisfies the inequality

$$\begin{cases} \dim(e \cap X_0) \leqslant \bar{p}(3) - 2 \\ \dim(e \cap (X_1 - X_0)) \leqslant \bar{p}(2) - 1 \\ \dim(e \cap (X_2 - X_1)) \leqslant \bar{p}(1) \end{cases} .$$

We check Figure 5-16 that the type III_1 intersects X_0 at 0 and intersects $X_1 - X_0$ at dimen-

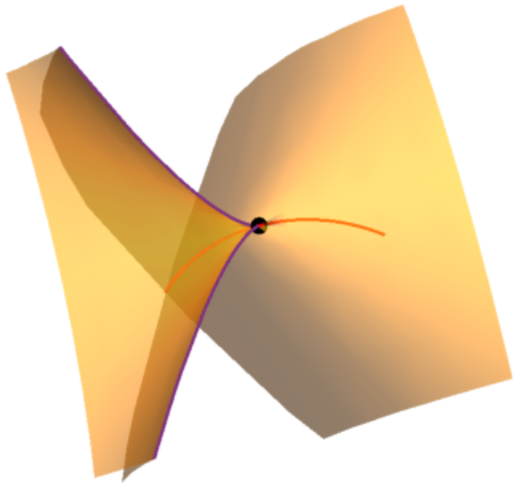

Figure 5-15 Filtration of swallowtail. $X_3 = \mathbb{R}^3$, X_2 is the yellow surface, X_1 is the red and purple intersection lines and X_0 is the origin point.

0-simplex:	type I_0 Only intersects with X_0
	type II_0 Only intersects with $X_1 - X_0$
	type III_0 Only intersects with $X_2 - X_1$
1-simplex:	type I_1 Only intersects with $X_1 - X_0$ at dim 1
	type II_1 Only intersects with $X_2 - X_1$ at dim 1
	type III_1 Intersects with X_0 at dim 0 and with $X_1 - X_0$ at dim 1
	type IV_1 Intersects with $X_3 - X_2$ at dim 1 and with $X_1 - X_0$ at dim 0
	type V Intersects with $X_2 - X_1$ at dim 1 and with $X_1 - X_0$ at dim 0
	type VI_1 Intersects with X_0 at dim 0 and with $X_2 - X_1$ at dim 1
	type VII_1 Intersects with $X_3 - X_2$ at dim 1 and with $X_2 - X_1$ at dim 0
	type $VIII_1$ Intersects with X_0 at dim 0 and with $X_3 - X_2$ at dim 1

Figure 5-16 Types of simplices.

sion 1. Taking the left hand side be 0 and 1 in the first and second equation, respectively, we have the type III_1 is allowable when $0 \leqslant \bar{p}(3) - 2$ and $\bar{p}(2) - 1 \geqslant 1$, i.e., $\bar{p}(3) \geqslant 2$ and $\bar{p}(2) \geqslant 2$, which is shown in Figure 5-17. Also, note that we omit the intersection at $X_3 - X_2$ since it's a regular stratum.

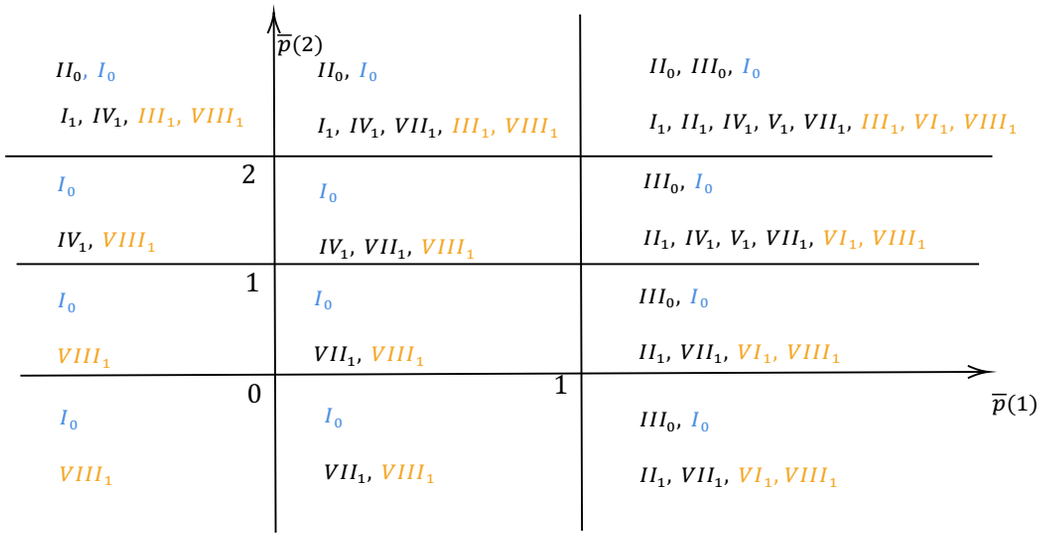

Figure 5-17 Regions corresponding to different allowable simplices under varying perversities. The yellow types are allowable when $\bar{p}(3) \geqslant 2$ and the blue ones are allowable when $\bar{p}(3) \geqslant 3$.

The computation is as following: To illustrate more explicitly, we divide the $\bar{p}(1)\bar{p}(2)\bar{p}(3)$-space into three regions. In the region A, the type IV_1 simplices are allowable, which means we can have path across singular lines X_1 to connect three connected components of $X_3 - X_2$; In the region B, the type VII_1 simplices are allowable, which means we can have path across singular surface $X_2 - X_1$ to connect three connected components of $X_3 - X_2$; In the region C with $\bar{p}(3) \geqslant 2$, the type $VIII_1$ simplices are allowable, which means we can have path across X_0 to connects the three connected components of $X_3 - X_2$; In the region C with $\bar{p}(3) < 2$, no simplices hitting singular part X_2 are allowable, hence we could see the three connected components of $X_3 - X_2$.

The degree-0 intersection homology=

$$\begin{cases} \mathbb{Z} \oplus \mathbb{Z} \oplus \mathbb{Z} & \text{if } \bar{p}(3) < 2, \bar{p}(2) < 1, \text{ and } \bar{p}(1) < 0 \\ \mathbb{Z} & \text{otherwise} \end{cases}.$$

0-degree intersection homology depict connected components. By regulating the three parameters, the degree 0 intersection group changes from $\mathbb{Z}$ to $\mathbb{Z} \oplus \mathbb{Z} \oplus \mathbb{Z}$, during which we detect the three regions Reg I, II, III, which are the three connected components of the complementary space of the swallowtail in $\mathbb{R}^3$, see Figure 5-15.

Figure 5-18 Division of the $\bar{p}(1)\bar{p}(2)\bar{p}(3)$-space into three parts.

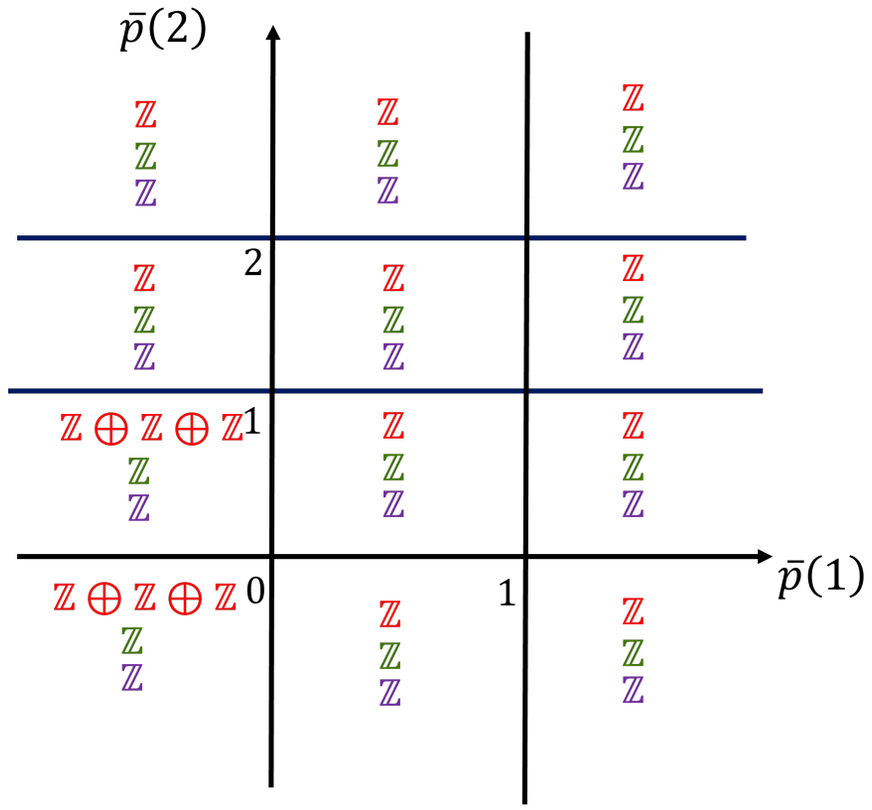

Figure 5-19 The degree-0 intersection homology of the swallowtail. Red corresponds to $\bar{p}(3) < 2$, green to $2 \leqslant \bar{p}(3) < 3$, and purple to $\bar{p}(3) \geqslant 3$.

The type of 2-simplex is in Table 5-1. The allowable 2 and 1-simplex for different perversity is shown in Figure 5-20. The computation is as following: Some important loops potentially could be generators of intersection homology groups; see Figure 5-21. Besides those loops, we also need to consider some loops that hit (not enclose) the singular spaces $X_2 - X_1$, $X_1 - X_0$, or X_0.

Table 5-1 Types of simplices

type I_2	Only intersects with $X_2 - X_1$ at dim 2
type II_2	Intersects with $X_3 - X_2$ at dim 2 and with X_0 at dim 0
type III_2	Intersects with $X_2 - X_1$ at dim 2 and with X_0 at dim 0
type IV_2	Intersects with $X_3 - X_2$ at dim 2 and with $X_1 - X_0$ at dim 1
type V_2	Intersects with $X_3 - X_2$ at dim 2 and with $X_1 - X_0$ at dim 0
type VI_2	Intersects with $X_2 - X_1$ at dim 2 and with $X_1 - X_0$ at dim 1
type VII_2	Intersects with $X_2 - X_1$ at dim 2 and with $X_1 - X_0$ at dim 0
type $VIII_2$	Intersects with $X_3 - X_2$ at dim 2 and with $X_2 - X_1$ at dim 1
type IX_2	Intersects with $X_3 - X_2$ at dim 2 and with $X_2 - X_1$ at dim 0
type X_2	Intersects with $X_2 - X_1$ at dim 2, with $X_1 - X_0$ at dim 1, and with X_0 at dim 0
type XI_2	Intersects with $X_3 - X_2$ at dim 2, with $X_2 - X_1$ at dim 1, and with X_0 at dim 0
type XII_2	Intersects with $X_3 - X_2$ at dim 2, with $X_1 - X_0$ at dim 1, and with X_0 at dim 0
type $XIII_2$	Intersects with $X_3 - X_2$ at dim 2, with $X_2 - X_1$ at dim 1, and with $X_1 - X_0$ at dim 0

To illustrte more explicitly, we divide the $\bar{p}(1)\bar{p}(2)\bar{p}(3)$-space into five regions, see Figure 5-22. In the region A, the allowable 1-cycle cannot traverse the singular surface at $X_2 - X_1$ but can hit X_1. Since the type V_2 and IV_2, the 1-cycle e is bounded. Hence, the intersection homology group is trivial. In the region B, no 1-cycles could hit X_2. However, the type V_2 is allowable, so the 1-cycle e is trivial. Hence, the intersection homology group is trivial. In the region C, no 1-cycles are allowed to transverse X_2. The 1-cycle e is allowed, but the type V_2 is not allowable, making e a generator of intersection homology. Hence, the intersection homology here is all $\mathbb{Z}$. In the region D, 1-cycles are allowed to transverse the singular surface X_2. The types $V_2, VIII_2, IX_2, XIII_2$ are allowed, and the 1-cycles a, b, c, d, e, f are all bounded, so the intersection homology group is trivial. In the region E with $\bar{p}(3) < 1$, the three 1-cycles a, b, c are all allowed and they are none trivial. Since types $VIII_2$ and IX_2 are allowed, $e = d = a + b + c$, which is also nontrivial. In the region E with $\bar{p}(3) \geqslant 1$, the type II_2 and XI_2 are allowable, making d (also e) being bounded. Hence the intersection here is $\mathbb{Z} \oplus \mathbb{Z} \oplus \mathbb{Z}/a + b + c$.

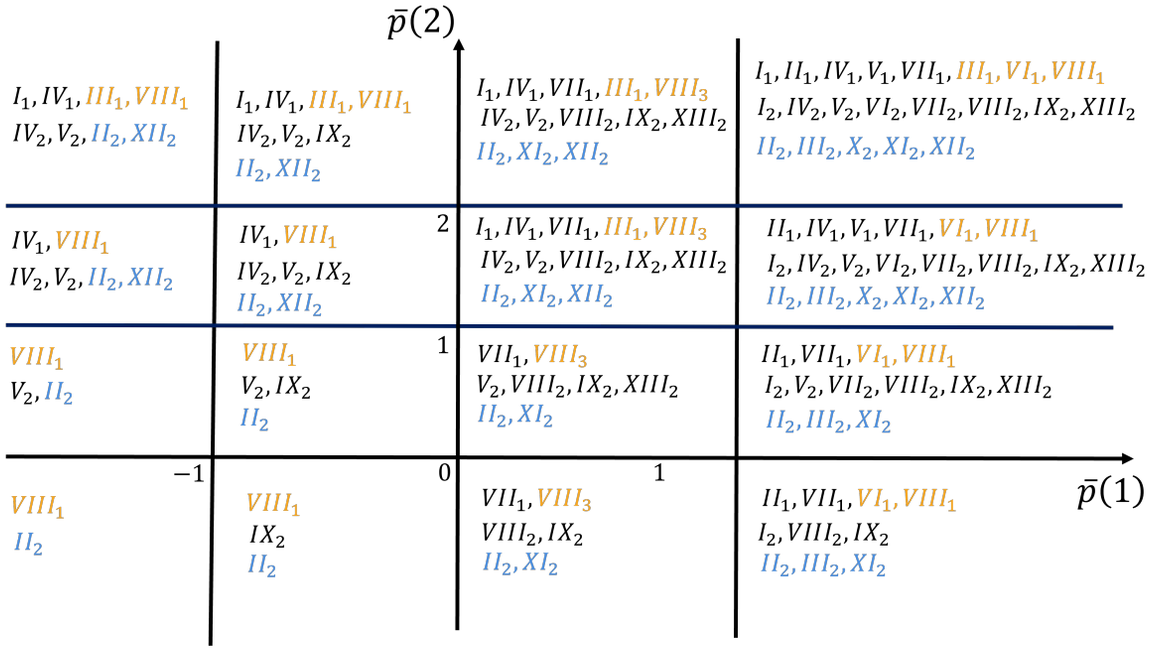

Figure 5-20 Regions corresponding to different allowable simplices under varying perversities. The blue is allowable when $\bar{p}(3) \geqslant 1$ and the yellow is allowable when $\bar{p}(3) \geqslant 2$.

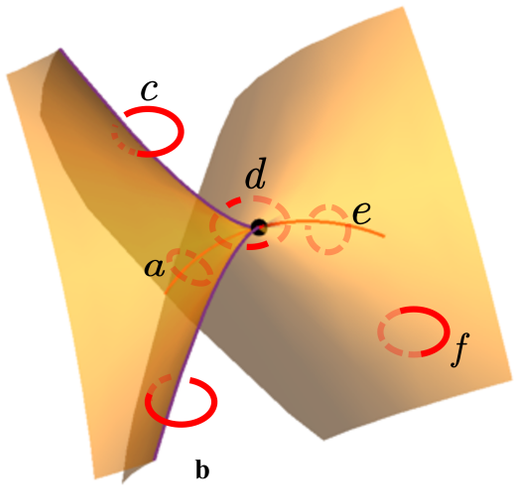

Figure 5-21 Some important loops. Loops a, b, and c enclose the singular lines on the surface, while loop e encloses the isolated singularity. Loop d is the composition of a, b, and c, surrounding the singular point at the origin. Loop f does not enclose any singular line.

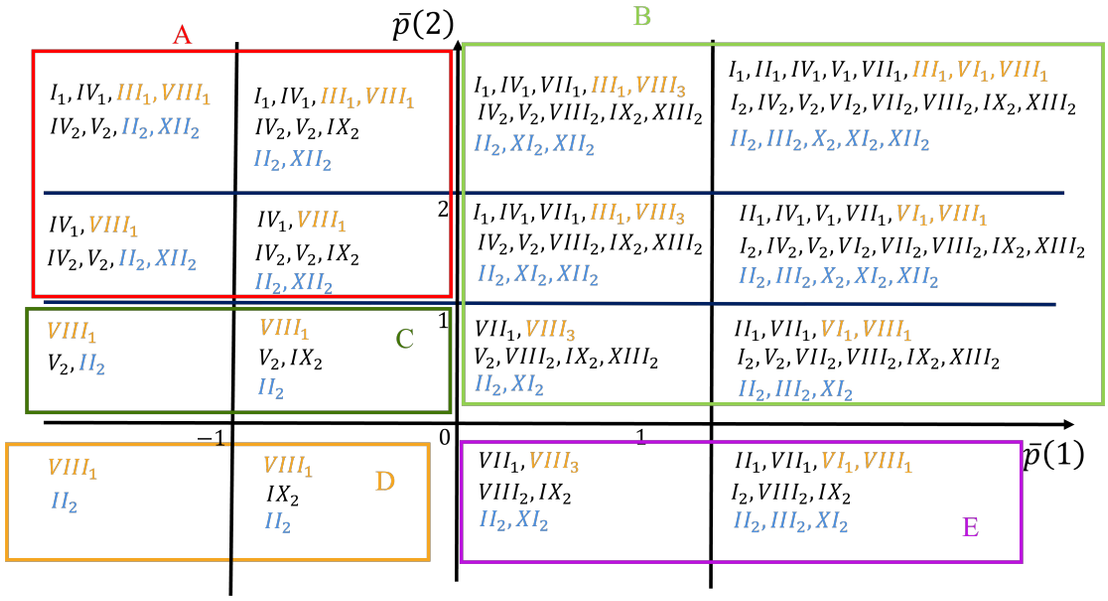

Figure 5-22 Division of the $\bar{p}(1)\bar{p}(2)\bar{p}(3)$-space into five parts.

The degree 1 intersection homology is shown in Figure 5-23, which can be formulated as: The degree-1 intersection homology=

$$\begin{cases} \mathbb{Z}e & \text{if } \forall \bar{p}(3) \in \mathbb{Z},\ \bar{p}(2) < 0, \text{ and } \bar{p}(1) < 0 \\ \mathbb{Z}a \oplus \mathbb{Z}b \oplus \mathbb{Z}c & \text{if } \bar{p}(3) < 1,\ \bar{p}(2) < 0, \text{ and } \bar{p}(1) \geqslant 0 \\ \mathbb{Z}a \oplus \mathbb{Z}b \oplus \mathbb{Z}c/a+b+c & \text{if } \bar{p}(3) \geqslant 1,\ \bar{p}(2) < 0, \text{ and } \bar{p}(1) \geqslant 0 \\ 0 & \text{otherwise} \end{cases},$$

where a, b, c are generators, shown in Figure 5-21.

Loops in Figure 5-21 satisfies conditions that $d = e = a+b+c$ in intersection groups containing a, b, c, d, e. These equations mean the three singular lines can fuse to the isolated singular lines. The group $\mathbb{Z}e$ detects the isolated singular line in the swallowtail but does not detect the three singular lines on the surface. The group $\mathbb{Z}a \oplus \mathbb{Z}b \oplus \mathbb{Z}c/a+b+c$ detects three singular lines on the surface but does not detect the isolated singular line since loop $e = d = 0$. The group $\mathbb{Z}a \oplus \mathbb{Z}b \oplus \mathbb{Z}c$ detects both the three singular lines on the surface and the isolated singular line since loop e equals d and $a+b+c$, which are nonzero. All the above shows that the isolated singular line strongly relates to the three singular lines on the surface.

The intersection cases of a 3-simplex can be classified by intersection dimension. The equivalence condition for those 3-simpleces being allowable is shown in Figure 5-24. The computation is as following: The possible nontrivial 2-cycles are the ones enclosing

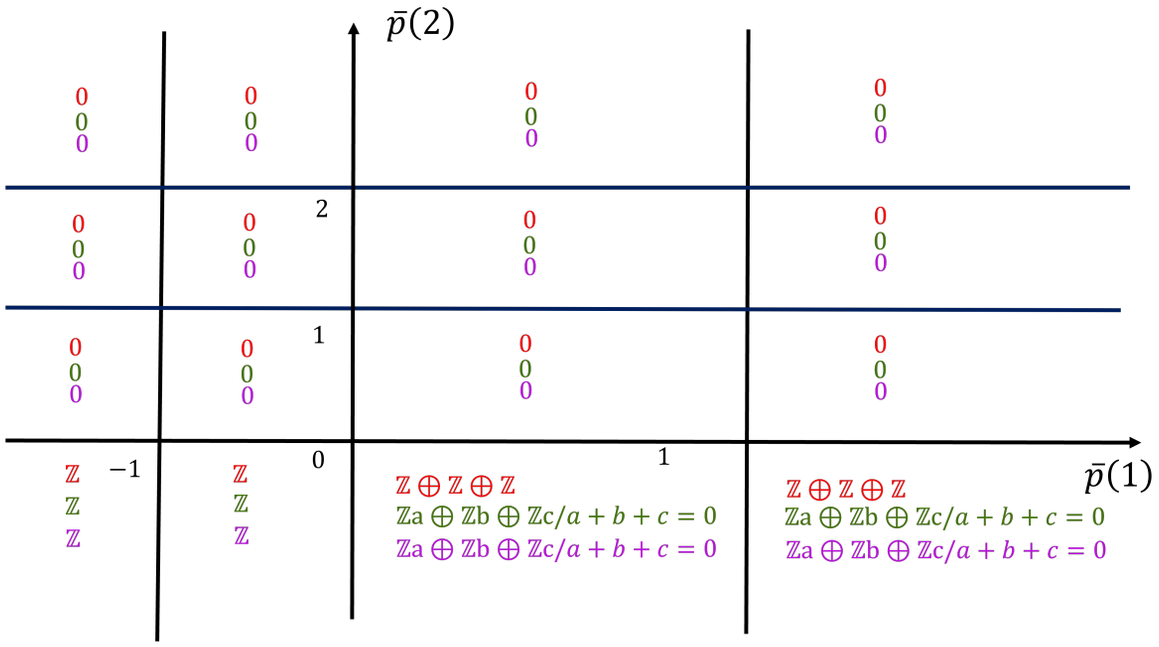

Figure 5-23 The degree-1 intersection homology of the swallowtail. The red region corresponds to $\bar{p}(3) < 1$, the green region to $1 \leqslant \bar{p}(3) < 2$, and the purple region to $\bar{p}(3) \geqslant 2$.

the origin, which need the type of 2-simplices that intersect with $X_1 - X_0$ at $\geqslant 0$ dimension and $X_2 - X_1$ at $\geqslant 1$ dimension. Therefore, for $\bar{p}(3) \geqslant 0$, the 3-simplex intersecting X_0 is allowed, so the intersection homology for $\bar{p}(3) \geqslant 0$ is all trivial, i.e., the green and purple ones in Figure 5-26 are all zero. To illustrte more explicitly, we divide the $\bar{p}(1)\bar{p}(2)\bar{p}(3)$-space into three regions, see Figure 5-25.

In the region A with $\bar{p}(3) < 0$, type V_2, $VIII_2$, IX_2 are allowable, so the 2-cycle enclose the origin are allowed. However, any 3-chain bounding it would have to intersect X_0, which is not allowed. Therefore, this cycle is nontrivial in intersection homology. Hence, the intersection group is $\mathbb{Z}$. In the region B, no allowable 2-cycles can transverse the singular surface X_2; thus, no 2-cycles can enclose the origin. Hence, the intersection homology here is zero. In the region C, no allowable 2-cycles can hit the singular line $X_1 - X_0$, so no 2-cycles can enclose the origin. Hence, the intersection homology here is zero.

The degree 2 intersection homology is shown in Figure 5-26, which can be formulated as: The degree-2 intersection homology=

$$\begin{cases} \mathbb{Z} & \text{if } \bar{p}(3) < 0,\ \bar{p}(2) \geqslant 0, \text{ and } \bar{p}(1) \geqslant 0 \\ 0 & \text{otherwise} \end{cases}.$$

The $\mathbb{Z}$ group is generated by a sphere enclosing the origin. Hence, during the degree 2 intersection group changing from 0 to $\mathbb{Z}$ by tuning parameters, we detect the singular

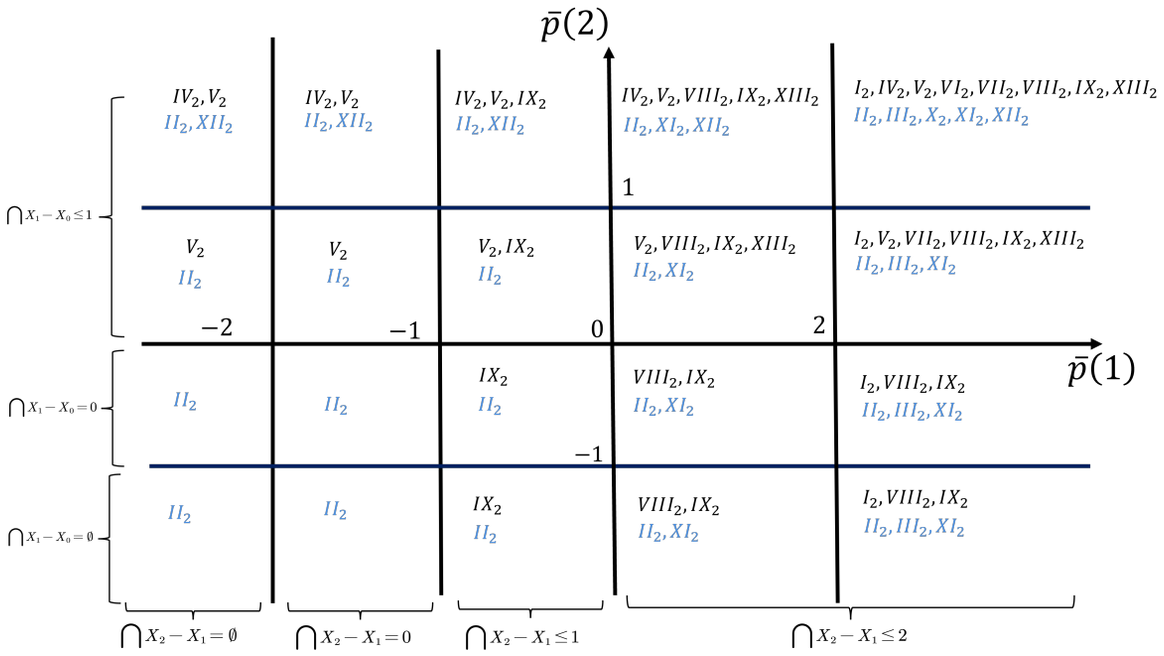

Figure 5-24 Allowable 2 and 3-simpleces for different perversity conditions. The blue ones are allowable when $\bar{p}(3) \geqslant 1$. The allowable 3-simplex with different intersection dimension condition are shown in the picture, e.g., the 3-simplex that does not intersect $X_2 - X_1$ is for $\bar{p}(1) < -2$. Note that the condition corresponds to whether 3-simplex could intersect the X_0 is not denoted in the picture. The 3-simplex intersect with X_0 is allowed only when $\bar{p}(3) \geqslant 0$.

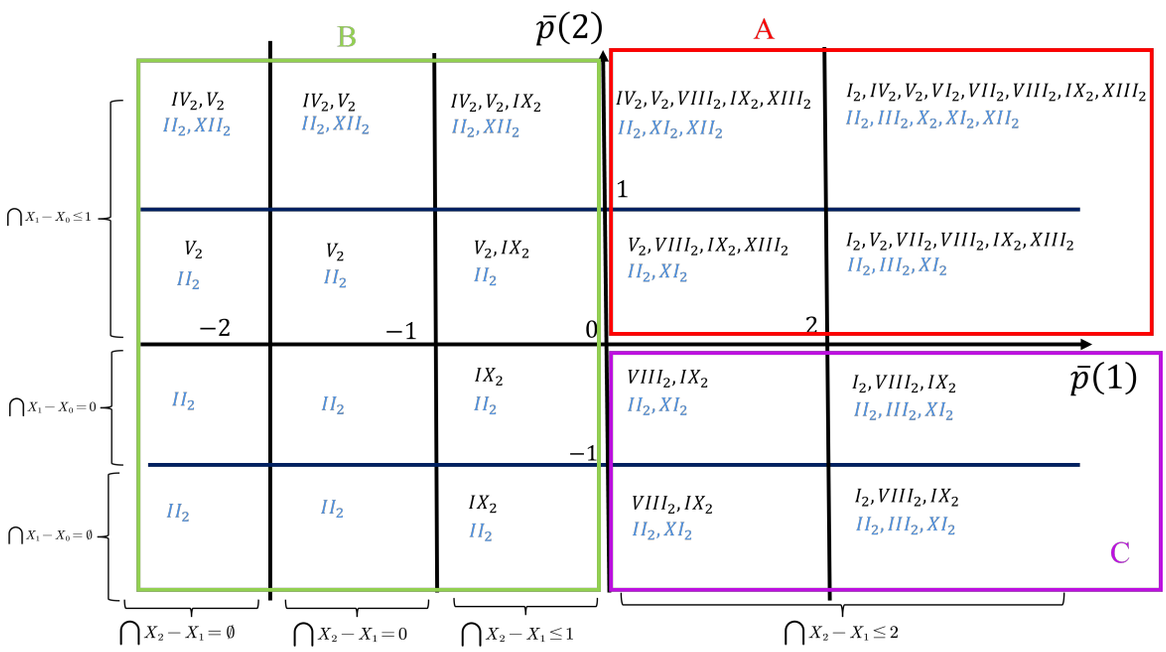

Figure 5-25 Division of the $\bar{p}(1)\bar{p}(2)\bar{p}(3)$-space into three parts.

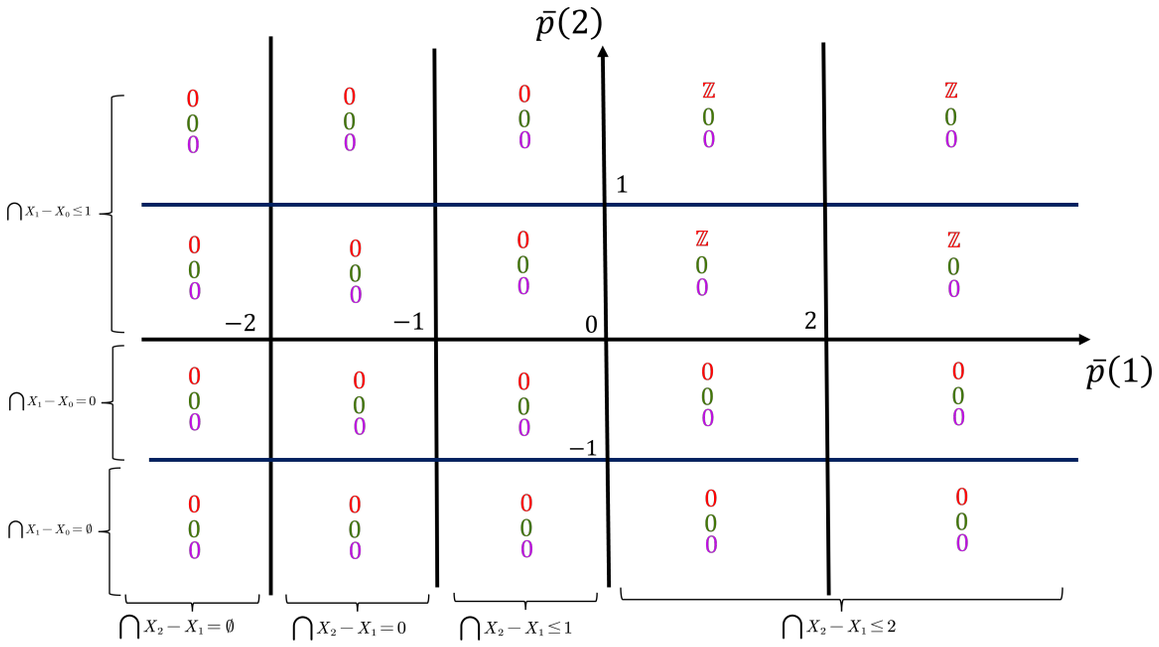

Figure 5-26 The degree-2 intersection homology of the swallowtail. The red region corresponds to $\bar{p}(3) < 0$, the green region to $0 \leqslant \bar{p}(3) < 1$, and the purple region to $\bar{p}(3) \geqslant 1$.

point MP (meeting point) at the origin.

Jing Hu et al. found that loop l_α can transition to l_β, that is, a pair of $EL3$s can transform into a NIL and an NL [29], see Figure 5-27. Our computation does not contradict this result. This is because, in intersection homology, the loops l_α and l_β belong to the same homology class. This phenomenon has also been verified experimentally. The authors built a special electric circuit to simulate a non-Hermitian system. By tuning control parameters, they measured how the energy levels evolve. They observed where energy levels meet and split, and found that two types of singular lines can transform into others, see Figure 5-28. They also tracked the evolution of states along a loop and found that the behavior remains the same. This shows that different singular lines are topologically connected.

5.5 An interesting phenomenon

By the results of intersection homology of $\mathbb{R}^2$ with a singular point at the origin, $\mathbb{R}^2$ with two singular lines, and swallowtail in $\mathbb{R}^3$, we find the following interesting phenomenon: It seems that the degree n intersection homology could only detect the $3-(n+1)$ dimensional singularities.

Firstly, we need to describe "detect" more explicitly. It is clear that if an n-chain encloses (not intersects with) a r-dimensional singularity and no $n+1$-chain with n-

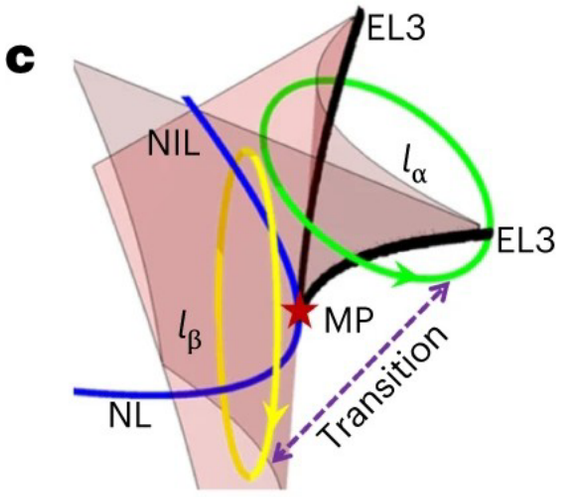

Figure 5-27 Transition of double $EL3$s to NIL and NL. (adapted from [29], Figure 4(c))

chain could intersect with a r-dimensional singularity for some perversity, we detect this singularity. For example, a sphere encloses the origin in the swallowtail example. These are all the cases in the above computations. Since an n-chain encloses an r-dimensional singularity, which means $r = 3-(n+1)$, it seems we describe the phenomenon. However, are there any other cases? For example, in Figure 5-29, the yellow surface is a singular surface, and the black 1-chain a intersects with these singular surfaces. If there is no allowable 2-chain with 1-chain a being a boundary, then this 1-chain is nontrivial and can detect the singular surface. However, it is impossible by the following property.

Proposition 5.5.1. For an allowable n-chain γ, if it intersects with a singular stratum S_i, where S_i has codimension i, and there exists $(n+1)$-chain η with $\partial\eta = \gamma$ and

$$\dim(\gamma \cap S_i) \geqslant \dim(\eta \cap S_i) - 1,$$

then γ is trivial.

Proof. Consider an allowable n-chain γ and $(n+1)$-chain η in $C_{n+1}(\mathbb{R}^3)$ with $\partial\eta = \gamma$. η may not be allowable, but we want to show η is allowable, i.e.,

$$\dim(\eta_j \cap S_i) \leqslant n + 1 - i + \bar{p}(i)$$

for each $(n+1)$-simplex η_j. Clearly, as a subspace, $\dim(\eta_j \cap S_i) \leqslant \dim(\eta \cap S_i)$ for each j. Consider the $(n+1)$-simplex η_{j_0} with $\dim(\eta_{j_0} \cap S_i) = \dim(\eta \cap S_i)$. If η_{j_0} is allowable, then

$$\dim(\eta_j \cap S_i) \leqslant \dim(\eta \cap S_i) = \dim(\eta_{j_0} \cap S_i) \leqslant n + 1 - i + \bar{p}(i)$$

for each j, complete the proof. Then we will show η_{j_0} is allowable.

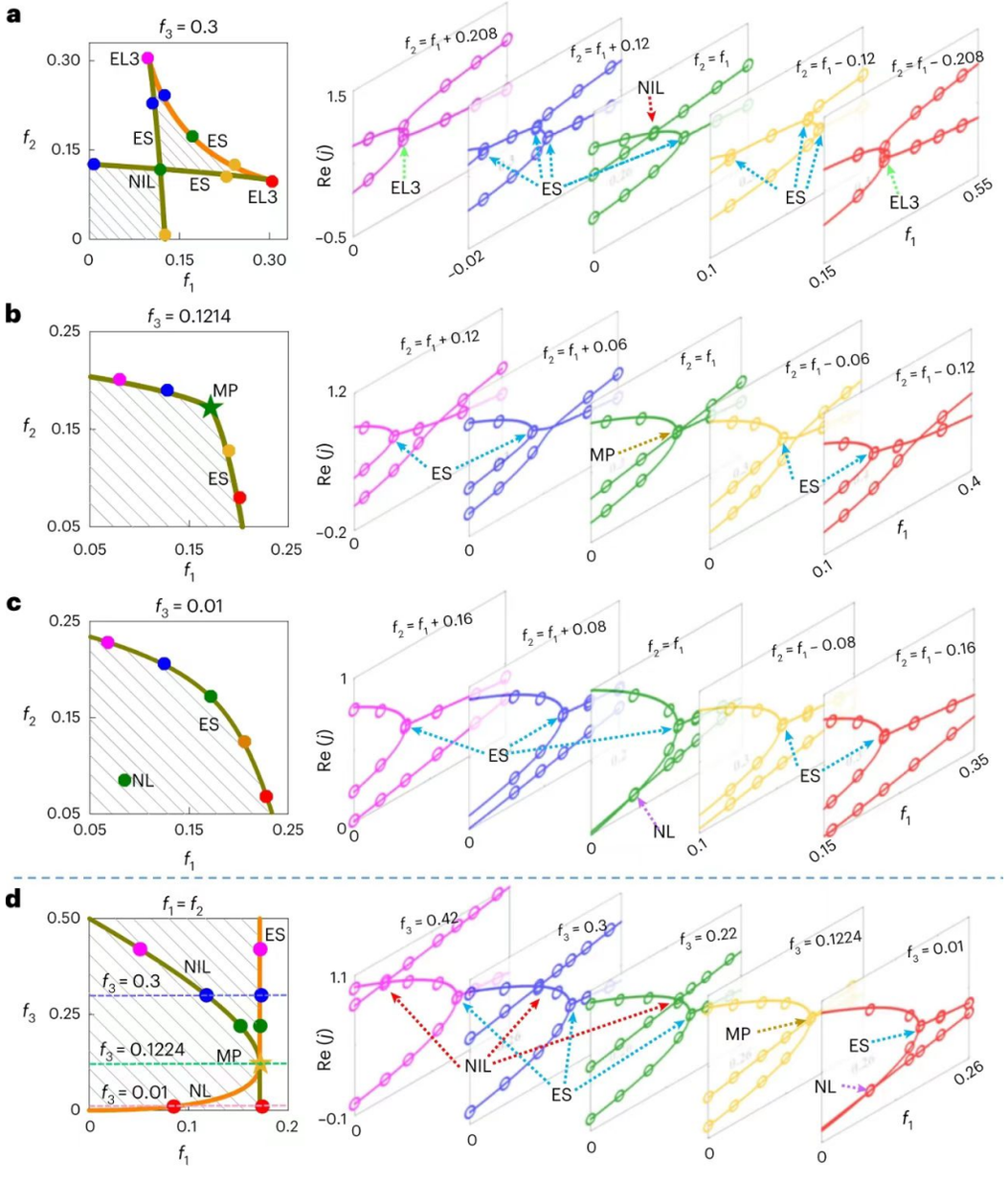

Figure 5-28 Experimental observation of the swallowtail catastrophe with the circuit system. (adapted from [29], Figure 3)

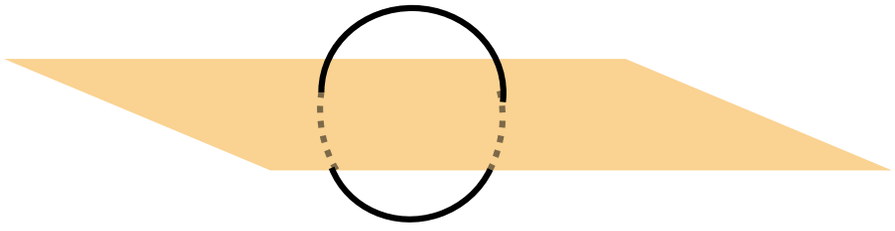

Figure 5-29 A possible nontrivial chain that does not enclose any singular lines.

Since γ is allowable, so for each n-simplex γ_k in γ, we have

$$\dim(\gamma_k \cap S_i) \leqslant n - i + \bar{p}(i).$$

As a subspace, we also have $\dim(\gamma_k \cap S_i) \leqslant \dim(\gamma \cap S_i)$ for each k. Let γ_{k_0} be the n-simplex in γ with $\dim(\gamma_{k_0} \cap S_i) = \dim(\gamma \cap S_i)$. Hence, we have

$$\dim(\gamma \cap S_i) = \dim(\gamma_{k_0} \cap S_i) \leqslant n - i + \bar{p}(i).$$

Then we obtain that $\bar{p}(i) \geqslant \dim(\gamma \cap S_i) - n + i$. Since $\dim(\gamma \cap S_i) \geqslant \dim(\eta \cap S_i) - 1$,

$$\bar{p}(i) \geqslant \dim(\eta \cap S_i) - n - 1 + i = \dim(\eta_{j_0} \cap S_i) - n - 1 + i.$$

, meaning that η_{j_0} is allowable.

Hence γ is bounded by η in the intersection homology, and thus γ is trivial.

Example 5.5.2. The 1-chain γ in Figure 5-29 must be trivial, since

$$\dim(\gamma \cap S_i) = 0 \geqslant \dim(\eta \cap S_i) = 1 - 1 = 0.$$

Remark 5.5.3. The condition $\dim(\gamma \cap S_i) \geqslant \dim(\eta \cap S_i) - 1$ holds for the most cases. Otherwise, $\dim(\gamma \cap S_i) \leqslant \dim(\eta \cap S_i) - 2$, which is ridiculous since $\dim(\eta) = \dim(\gamma) + 1$.

Note that we discuss the cases where γ intersects with only one stratum. It can also be generalized to the case where γ intersects with finitely many strata.

Corollary 5.5.4. Let γ be an allowable n-chain intersecting with

$$\{S_i^1, \cdots, S_i^{n_i} \mid i \in I, n_i \in \mathbb{N}\},$$

where I is some index set. If there exists an $(n+1)$-chain η with $\partial\eta = \gamma$ and $\dim(\gamma \cap S_i^l) \geqslant \dim(\eta \cap S_i^l) - 1$ for all $i \in I$ and $1 \leqslant l \leqslant n_i$, then γ is trivial.

CONCLUSION

The problem contains 2-band Hermitian/pseudo-Hermitian and 3-band Hermitian/pseudo-Hermitian.

A 2-band Hermitian has three ways of classifying. A 2-band Hermitian matrix is

$$A\,(l,s,t) = \begin{bmatrix} l+t & s \\ s & l-t \end{bmatrix},$$

The eigenbundle is the Hopf bundle $S^0 \to S^1 \to S^1$ [32]. The result is that any loops enclosing $\hat{l}$-axis are a Hopf bundle, while loops not enclosing $\hat{l}$-axis are trivial. Following [34], the Berry phase of a spin in a magnetic field is $\gamma = -\frac{1}{2}\Omega$. In this work, we use the matrix $A(l,s,t)$ to study this effect. We show that different loops in parameter space match the physics: a loop that goes around $\hat{l}$ once gives a nontrivial phase, a loop that does not go around $\hat{l}$ gives zero phase, and a loop that goes around $\hat{l}$ twice is again trivial. This means our topological classification agrees with the physical result. The second way is that we can classify it by computing the fundamental group of the order parameter [28], the fundamental group $\pi_1(S^1) = \mathbb{Z}$. The third way is that we can classify it by computing $\pi_1(\mathrm{SO}(2)/\mathrm{O}(1))$. We can visualize the evolution of eigenvectors on a loop by the ball method.

For the 2-band pseudo-Hermitian, it has the form

$$H = \begin{bmatrix} a & b \\ -b & c \end{bmatrix}, \quad a,b,c \in \mathbb{R},$$

and H has the following symmetries:

$$v_{\pm}(a+s,b,c+s) = v_{\pm}(a,b,c)$$

and

$$v_{\pm}(ka,kb,kc) = v_{\pm}(a,b,c), k \neq 0.$$

So we can always reduce three parameters to 1 parameter. Hence, we can visualize the evolution of two eigenvectors in the particular case when $a = -c$.

3-band Hermitian has two ways to classify. The eigenbundles can be described by

the bundle

$$\mathrm{D}_2 \longrightarrow \mathrm{SO}(3) \longrightarrow \mathrm{SO}(3)/\mathrm{D}_2.$$

The classifying map

$$\phi : \mathrm{SO}(3)/\mathrm{D}_2 \longrightarrow Gr_1(\mathbb{R}^\infty) \times Gr_1(\mathbb{R}^\infty)$$

is given by

$$\phi\left(\left[\begin{matrix} l \\ s \\ t \end{matrix}\right]\right) = \left(\mathrm{span}\begin{pmatrix} l & 0 & 0 & \cdots \end{pmatrix}, \mathrm{span}\begin{pmatrix} s & 0 & 0 & \cdots \end{pmatrix}\right).$$

The second way is that we can classify by the fundamental group $\pi_1(\mathrm{SO}(3)/\mathrm{D}_2)$. We can visualize the evolution of eigenvectors on a loop by the ball method.

The other main result of this paper is the computation of intersection homology.

Intersection homology of $\mathbb{R}^2$ with a singular point at the origin is shown in Figure 5-30. From the yellow region to the green region, the $I^{\bar{p}}H_1(\mathbb{R}^2)$ varies from 0 to $\mathbb{Z}$, meaning that we detect the singular point at the origin.

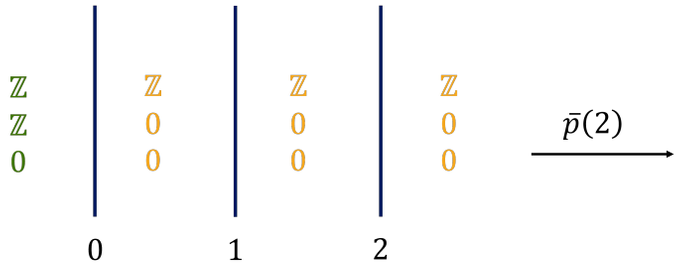

Figure 5-30 Intersection homology of $\mathbb{R}^2$ with one singular point:from top to bottom is $I^{\bar{p}}H_0$, $I^{\bar{p}}H_1$, $I^{\bar{p}}H_2$.

Intersection homology of $\mathbb{R}^2$ with two singular lines is shown in Figure 5-31. In Figure 5-31, from yellow region to green region, we "see" the two singular lines; From yellow region to red region, we "see" the singular point at the origin. It's equal to regular homology $H_*(\mathbb{R}^2)$ for nonnegative perversity.

The following is the intersection homology of a swallowtail in $\mathbb{R}^3$.

The degree-0 intersection homology=

$$\begin{cases} \mathbb{Z} \oplus \mathbb{Z} \oplus \mathbb{Z} & \text{if } \bar{p}(1) < 0,\ \bar{p}(2) < 1, \text{ and } \bar{p}(3) < 2 \\ \mathbb{Z} & \text{otherwise} \end{cases}.$$

0-degree intersection homology depict connected components. By tuning the three parameters, the degree 0 intersection group changes from $\mathbb{Z}$ to $\mathbb{Z} \oplus \mathbb{Z} \oplus \mathbb{Z}$, during which

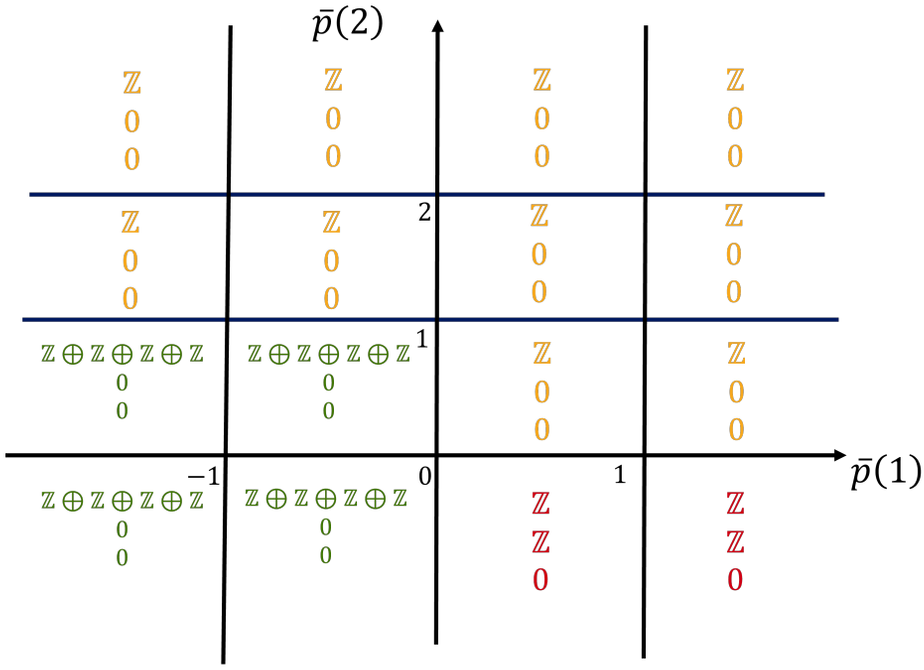

Figure 5-31 Intersection homology of $\mathbb{R}^2$ with two singular lines. From top to bottom is $I^{\bar{p}}H_0$, $I^{\bar{p}}H_1$, $I^{\bar{p}}H_2$.

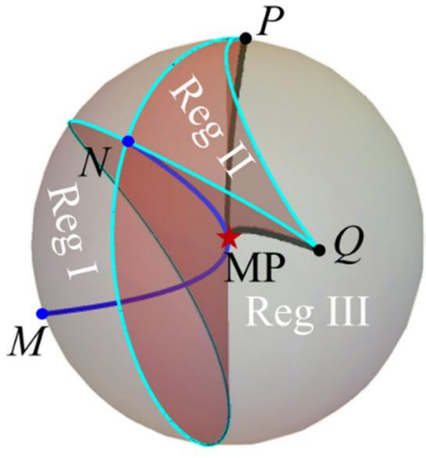

Figure 5-32 Three connected components, Reg I, II, III of the complementary space of the swallowtail in $\mathbb{R}^3$, adapted from [29], Figure S7.

we detect the three regions Reg I, II, III, which are the three connected components of the complementary space of the swallowtail in $\mathbb{R}^3$, see Figure 5-32.

The degree-1 intersection homology=

$$\begin{cases} \mathbb{Z}e & \text{if } \bar{p}(1) < 0,\ \bar{p}(2) < 0,\ \text{and } \forall \bar{p}(3) \in \mathbb{Z} \\ \mathbb{Z}a \oplus \mathbb{Z}b \oplus \mathbb{Z}c & \text{if } \bar{p}(1) \geqslant 0,\ \bar{p}(2) < 0,\ \text{and } \bar{p}(3) < 1 \\ \mathbb{Z}a \oplus \mathbb{Z}b \oplus \mathbb{Z}c/a+b+c & \text{if } \bar{p}(1) \geqslant 0,\ \bar{p}(2) < 0,\ \text{and } \bar{p}(3) \geqslant 1 \\ 0 & \text{otherwise} \end{cases},$$

where a, b, c are generators, shown in Figure 5-33.

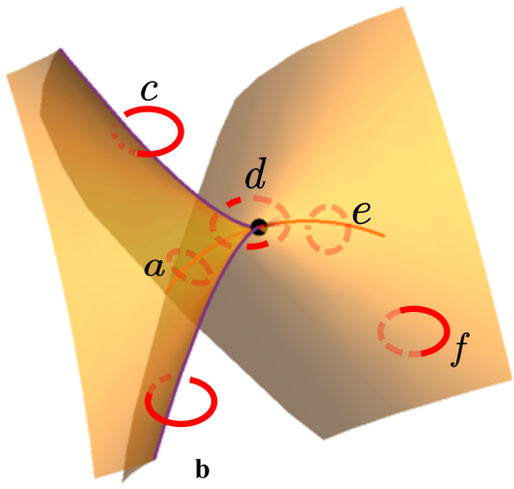

Figure 5-33 Some important loops. Loops a, b, and c enclose the singular lines on the surface, while loop e encloses the isolated singularity. Loop d is the composition of a, b, and c, surrounding the singular point at the origin. Loop f does not enclose any singular line.

Loops in Figure 5-33 are satisfying $a+b+c=d$, $d=e$ in intersection groups containing a, b, c, d, e. These equations mean the three singular lines can fuse to the isolated singular lines. The group $\mathbb{Z}e$ detects the isolated singular line in the swallowtail but does not detect the three singular lines on the surface. The group $\mathbb{Z}a \oplus \mathbb{Z}b \oplus \mathbb{Z}c/(a+b+c=0)$ detects three singular lines on the surface but does not detect the isolated singular line since loop $e = d = 0$. The group $\mathbb{Z}a \oplus \mathbb{Z}b \oplus \mathbb{Z}c$ detects both the three singular lines on the surface and the isolated singular line since loop $e = d = a + b + c \neq 0$. All the above shows that the isolated singular line strongly relates to the three singular lines on the surface.

The degree-2 intersection homology=

$$\begin{cases} \mathbb{Z} & \text{if } \bar{p}(1) \geqslant 0,\ \bar{p}(2) \geqslant 0, \text{ and } \bar{p}(3) < 0 \\ 0 & \text{otherwise} \end{cases}.$$

The $\mathbb{Z}$ group is generated by a sphere enclosing the origin. Hence, during the degree 2 intersection group changing from 0 to $\mathbb{Z}$ by tuning parameters, we detect the singular point MP (meeting point) at the origin.

During the computation, I proved the following useful tools to judge whether an allowable chain is trivial or not. For an allowable n-chain γ, if it intersects with a singular stratum S_i, where S_i has codimension i, and there exists $(n+1)$-chain η with $\partial\eta = \gamma$ and $\dim(\gamma \cap S_i) \geqslant \dim(\eta \cap S_i) - 1$, then γ is trivial. This can be generalized to: Let γ be an allowable n-chain intersecting with $\{S_i^1, \cdots, S_i^{n_i} \mid i \in I, n_i \in \mathbb{N}\}$, where I is some index set. If there exists an $(n+1)$-chain η with $\partial\eta = \gamma$ and $\dim(\gamma \cap S_i^l) \geqslant \dim(\eta \cap S_i^l) - 1$ for all $i \in I$ and $1 \leqslant l \leqslant n_i$, then γ is trivial.

REFERENCES

[1] XUE W T, HU Y M, SONG F, et al. Non-Hermitian Edge Burst[J/OL]. Phys. Rev. Lett., 2022, 128: 120401. https://link.aps.org/doi/10.1103/PhysRevLett.128.120401.

[2] ZHANG X Z, ZHANG G, SONG Z. Classical correspondence of the exceptional points in the finite non-Hermitian system[J/OL]. Journal of Physics A: Mathematical and Theoretical, 2019, 52(16): 165302. https://doi.org/10.1088/1751-8121/ab0ede.

[3] LI L, LEE C H, GONG J. Geometric characterization of non-Hermitian topological systems through the singularity ring in pseudospin vector space[J/OL]. Phys. Rev. B, 2019, 100: 075403. https://link.aps.org/doi/10.1103/PhysRevB.100.075403.

[4] YANG S B, HAN P R, NING W, et al. An exceptional surface and its topology[J/OL]. Science China Physics, Mechanics & Astronomy, 2026, 69(3): 230313. https://doi.org/10.1007/s11433-025-2851-8.

[5] JIA H, HU J, ZHANG R Y, et al. Unconventional Topological Edge States In One-Dimensional Non-Hermitian Gapless Systems Stemming from Nonisolated Hypersurface Singularities[J/OL]. Phys. Rev. Lett., 2025, 134: 206603. https://link.aps.org/doi/10.1103/PhysRevLett.134.206603.

[6] LEE C H, LI L, THOMALE R, et al. Unraveling non-Hermitian pumping: Emergent spectral singularities and anomalous responses[J/OL]. Phys. Rev. B, 2020, 102: 085151. https://link.aps.org/doi/10.1103/PhysRevB.102.085151.

[7] OZAWA T, PRICE H M, AMO A, et al. Topological photonics[J/OL]. Rev. Mod. Phys., 2019, 91: 015006. https://link.aps.org/doi/10.1103/RevModPhys.91.015006.

[8] TANG W, DING K, MA G. Direct Measurement of Topological Properties of an Exceptional Parabola[J/OL]. Phys. Rev. Lett., 2021, 127: 034301. https://link.aps.org/doi/10.1103/PhysRevLett.127.034301.

[9] HU H, SUN S, CHEN S. Knot topology of exceptional point and non-Hermitian no-go theorem [J/OL]. Phys. Rev. Res., 2022, 4: L022064. https://link.aps.org/doi/10.1103/PhysRevResearch.4.L022064.

[10] HAJONG G, MODAK R, MANDAL B P. Emergence of Hermitian topology from non-Hermitian knots[J/OL]. Phys. Rev. B, 2026, 113(11): 115406. DOI: 10.1103/x749-t8g6.

[11] YANG Y, YANG B, MA G, et al. Non-Abelian physics in light and sound[J/OL]. Science, 2024, 383(6685): eadf9621. https://www.science.org/doi/abs/10.1126/science.adf9621.

[12] DOUWES T, STÅLHAMMAR M. Twisted (co)homology of non-orientable Weyl semimetals [A]. 2025. arXiv: 2511.22303.

[13] STÅLHAMMAR M, RØDLAND L. Abelian spectral topology of multifold exceptional points [J/OL]. Phys. Rev. Res., 2025, 7: 033246. https://link.aps.org/doi/10.1103/8lyx-vtnw.

[14] DELPLACE P, YOSHIDA T, HATSUGAI Y. Symmetry-Protected Multifold Exceptional Points and Their Topological Characterization[J/OL]. Phys. Rev. Lett., 2021, 127: 186602. https://link.aps.org/doi/10.1103/PhysRevLett.127.186602.

[15] TANG W, DING K, MA G. Realization and topological properties of third-order exceptional lines embedded in exceptional surfaces[J/OL]. Nature Communications, 2023, 14(1): 6660. https://doi.org/10.1038/s41467-023-42414-z.

[16] YOSHIDA T, KÖNIG J L K, RØDLAND L, et al. Winding topology of multifold exceptional points[J/OL]. Phys. Rev. Res., 2025, 7: L012021. https://link.aps.org/doi/10.1103/PhysRevResearch.7.L012021.

[17] RYU J W, HAN J H, YI C H. Classification of multiple arbitrary-order non-Hermitian singularities[J/OL]. Phys. Rev. A, 2022, 106: 012218. https://link.aps.org/doi/10.1103/PhysRevA.106.012218.

[18] TLUSTY T. Exceptional topology in ordinary soft matter[J/OL]. Phys. Rev. E, 2021, 104: 025002. https://link.aps.org/doi/10.1103/PhysRevE.104.025002.

[19] MONKMAN K, SIRKER J. Hidden Zero Modes and Topology of Multiband Non-Hermitian Systems[J/OL]. Phys. Rev. Lett., 2025, 134: 056601. https://link.aps.org/doi/10.1103/PhysRevLett.134.056601.

[20] HERVIOU L, BARDARSON J H, REGNAULT N. Defining a bulk-edge correspondence for non-Hermitian Hamiltonians via singular-value decomposition[J/OL]. Phys. Rev. A, 2019, 99: 052118. https://link.aps.org/doi/10.1103/PhysRevA.99.052118.

[21] RAMOS T, GARCÍA-RIPOLL J J, PORRAS D. Topological input-output theory for directional amplification[J/OL]. Phys. Rev. A, 2021, 103: 033513. https://link.aps.org/doi/10.1103/PhysRevA.103.033513.

[22] BRUNELLI M, WANJURA C C, NUNNENKAMP A. Restoration of the non-Hermitian bulk-boundary correspondence via topological amplification[J/OL]. SciPost Phys., 2023, 15(4): 173. DOI: 10.21468/SciPostPhys.15.4.173.

[23] PORRAS D, FERNÁNDEZ-LORENZO S. Topological Amplification in Photonic Lattices [J/OL]. Phys. Rev. Lett., 2019, 122: 143901. https://link.aps.org/doi/10.1103/PhysRevLett.122.143901.

[24] WANJURA C C, NUNNENKAMP A. Unifying framework for non-Hermitian and Hermitian topology in driven-dissipative systems[A]. 2025. arXiv: 2509.19433.

[25] JIA H, HU J, ZHANG R Y, et al. Non-Hermitian swallowtail catastrophe revealing transitions across diverse topological singularities[EB/OL]. 2022. DOI: 10.21203/rs.3.rs-1853770/v1.

[26] WU Q, SOLUYANOV A A, BZDUŠEK T. Non-Abelian band topology in noninteracting metals [J/OL]. Science, 2019, 365: 1273-1277. DOI: 10.1126/science.aau8740.

[27] WOJCIK C C, SUN X Q, BZDUŠEK T, et al. Homotopy characterization of non-Hermitian Hamiltonians[J/OL]. Phys. Rev. B, 2020, 101: 205417. https://link.aps.org/doi/10.1103/PhysRevB.101.205417.

[28] MERMIN N D. The topological theory of defects in ordered media[J/OL]. Rev. Mod. Phys., 1979, 51: 591-648. https://link.aps.org/doi/10.1103/RevModPhys.51.591.

[29] HU J, ZHANG R Y, WANG Y, et al. Non-Hermitian swallowtail catastrophe revealing transitions among diverse topological singularities[J/OL]. Nature Physics, 2023, 19: 1098-1103. DOI: 10.1038/s41567-023-02048-w.

[30] TAUBER C, DELPLACE P, VENAILLE A. Anomalous bulk-edge correspondence in continuous media[J/OL]. Phys. Rev. Res., 2020, 2: 013147. https://link.aps.org/doi/10.1103/PhysRevResearch.2.013147.

[31] JIA H, ZHANG R Y, HU J, et al. Topological classification for intersection singularities of exceptional surfaces in pseudo-Hermitian systems[J/OL]. Communications Physics, 2023, 6 (1): 293. https://doi.org/10.1038/s42005-023-01417-4.

[32] ROOS B, FELDER G. [C/OL]//Principal bundles, Hopf bundles and Eigenbundles. 2022. https://api.semanticscholar.org/CorpusID:252335927.

[33] 尤承业. 基础拓扑学讲义[M]. 北京: 北京大学出版社, 1997: 63.

[34] GRIFFITHS D J, SCHROETER D F. Introduction to Quantum Mechanics[M]. 3rd ed. Cambridge University Press, 2018.

[35] FRIEDMAN G. Singular chain intersection homology for traditional and super-perversities [J/OL]. Transactions of the American Mathematical Society, 2004, 359: 1977-2019. https://api.semanticscholar.org/CorpusID:12243329.

[36] WRAZIDLO D J. A Fundamental Class for Intersection Spaces of Depth One Witt Spaces [J/OL]. manuscripta mathematica, 2019, 166: 199 - 236. https://api.semanticscholar.org/CorpusID:102350621.

[37] FRIEDMAN G. Intersection homology Künneth theorems[J/OL]. Mathematische Annalen, 2008, 343: 371-395. https://api.semanticscholar.org/CorpusID:2064206.

[38] FRIEDMAN G. New Mathematical Monographs: Singular Intersection Homology[M]. Cambridge University Press, 2020.

[39] DEOPURKAR A. An introduction to intersection homology[EB/OL]. 2010. https://deopurkar.github.io/papers/anandrd_minor_thesis.pdf.

[40] MAXIM L G. Graduate Texts in Mathematics: Vol. 281 Intersection Homology & Perverse Sheaves: with Applications to Singularities[M/OL]. Cham: Springer, 2019. DOI: 10.1007/978-3-030-27644-7.

[41] CHATAUR D, SARALEGI-ARANGUREN M, TANRé D. Relation between intersection homology and homotopy groups[J/OL]. Journal of the European Mathematical Society, 2025. http://dx.doi.org/10.4171/JEMS/1625. DOI: 10.4171/jems/1625.

ACKNOWLEDGEMENTS

First of all, I would like to give my heartfelt thanks to my supervisor, Yifei Zhu, for his kind guidance through the difficulties with this problem. I am also extremely grateful to my pre-supervisor, Liang Kong. Without his encouragement, I would never have known what I truly want to pursue.

My sincere and hearty thanks and appreciation go to Chenlu Huang, Qingrui Qu, Wenhui Yang, and Zhiwang Yu; without their discussions, this thesis would not have been possible.

In addition, many thanks go to my family who love and care for me and whom I love and care for.

And my warm gratitude also goes to my friends Xinyu Chen, Yiming Chen, Hao Fang, Hui Guo, Chenlu Huang, Xiaoyu Liu, and Zongnan Zhang. They erase my anxiety and raise me in the tough times during my master's degree. Moreover, I wish to extend my thanks to friends in the Kungfu society and the Kayak team, who shared a meaningful experience that made me stronger both physically and mentally.

Finally, my cordial thanks also go to my toy dog, who compares with me every day.

RESUME AND ACADEMIC ACHIEVEMENTS

Resume

Zhou Fang was born in 2001, in Wenzhou, Zhejiang, China.

In September 2019, she was admitted to Southern University of Science and Technology (SUSTech). In June 2023, she obtained a bachelor's degree in physics from the Department of Physics, SUSTech.

Since September 2023, she has started to pursue her master's degree of Quantum Science and Engineering in Institute of Quantum Science and Engineering, SUSTech.

Academic Achievements during the Study for an Academic Degree

No published articles yet.